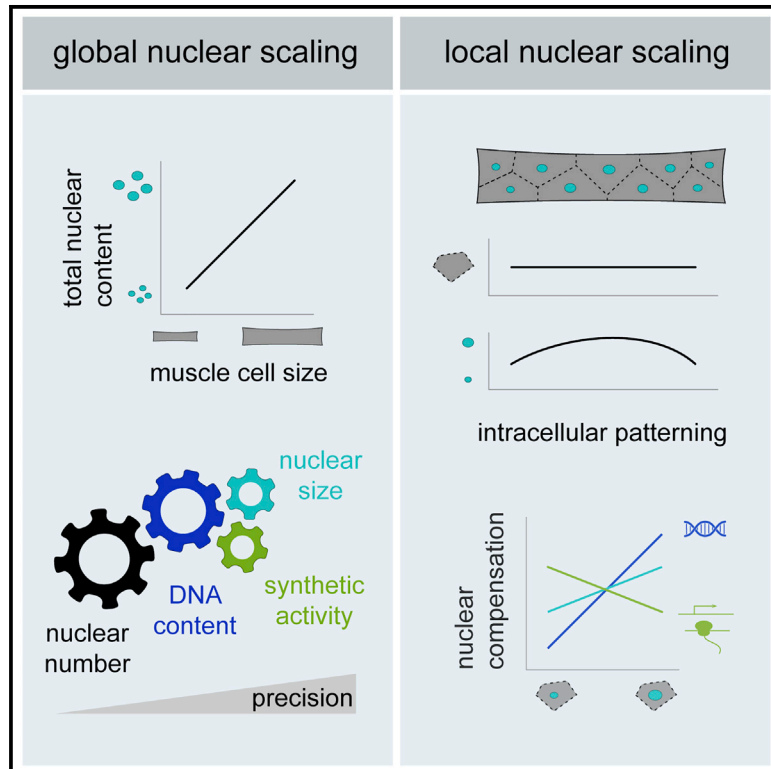


Developmental Cell

Nuclear Scaling Is Coordinated among Individual Nuclei in Multinucleated Muscle Fibers

Graphical Abstract



Authors

Stefanie E. Windner, Angelika Manhart, Amelia Brown, Alex Mogilner, Mary K. Baylies

Correspondence

m-baylies@ski.mskcc.org

In Brief

Muscle fibers are large multinucleated cells with remarkable size plasticity. Windner et al. investigate the relationship between muscle cell size and nuclear content. They show that cells contain a heterogeneous population of nuclei and explore mechanisms of nuclear coordination, as well as the functional consequences of scaling perturbations.

Highlights

- Muscle nuclei collectively establish precise global scaling with muscle fiber size
- Cells contain domains with distinct local scaling of DNA, nuclear and nucleolar sizes
- Nucleolar scaling indicates proportionally higher synthetic activity in small nuclei
- Changes in DNA content affect nuclear scaling relationships and muscle function



Nuclear Scaling Is Coordinated among Individual Nuclei in Multinucleated Muscle Fibers

Stefanie E. Windner,¹ Angelika Manhart,² Amelia Brown,¹ Alex Mogilner,² and Mary K. Baylies^{1,3,*}

¹Developmental Biology Program, Sloan Kettering Institute, Memorial Sloan Kettering Cancer Center, New York, NY 10065, USA

²Courant Institute, New York University, New York, NY 10012, USA

³Lead Contact

*Correspondence: m-baylies@ski.mskcc.org

<https://doi.org/10.1016/j.devcel.2019.02.020>

SUMMARY

Optimal cell performance depends on cell size and the appropriate relative size, i.e., scaling, of the nucleus. How nuclear scaling is regulated and contributes to cell function is poorly understood, especially in skeletal muscle fibers, which are among the largest cells, containing hundreds of nuclei. Here, we present a *Drosophila in vivo* system to analyze nuclear scaling in whole multinucleated muscle fibers, genetically manipulate individual components, and assess muscle function. Despite precise global coordination, we find that individual nuclei within a myofiber establish different local scaling relationships by adjusting their size and synthetic activity in correlation with positional or spatial cues. While myonuclei exhibit compensatory potential, even minor changes in global nuclear size scaling correlate with reduced muscle function. Our study provides the first comprehensive approach to unraveling the intrinsic regulation of size in multinucleated muscle fibers. These insights to muscle cell biology will accelerate the development of interventions for muscle diseases.

INTRODUCTION

The physical dimensions of a cell and the appropriate relative size of its organelles are essential for cell structure and function. Cell size and intracellular scaling relationships are established and actively maintained in a cell-type-specific manner by integrating both extrinsic and intrinsic signals. Extrinsic size regulation includes systemic factors such as nutrition, insulin signaling, and hormones, which determine organ and overall body size by regulating cell numbers and sizes (Boulan et al., 2015; Penzo-Méndez and Stanger, 2015). Intrinsically, individual cells continuously assess their size in relation to their target size and adjust their growth and synthetic activity rates to optimize cell function (Amodeo and Skotheim, 2016; Chan and Marshall, 2012; Ginzberg et al., 2015). While the molecular mechanisms of systemic cell size regulation are rather well characterized, less is known about the intrinsic side.

Intrinsic regulators of cell size include DNA content, nuclear size, and nuclear activity (Frawley and Orr-Weaver, 2015; Miettinen et al., 2014; Mukherjee et al., 2016). The amount of nuclear DNA shows a coarse correlation with cell size (e.g., diploid cardiomyocytes are smaller than polyploid ones); however, different diploid cell types within the same organism establish a wide variety of cell and nuclear sizes (Gillooly et al., 2015). In contrast, each cell type can be characterized by a specific ratio of nuclear to cytoplasmic volume (nuclear size scaling) (Conklin, 1912). The precise regulation of nuclear size affects DNA organization, transcriptional and translational processes, nuclear import and export, and transport and diffusion of products throughout the cytoplasm (Levy and Heald, 2012). Further, nuclear size scaling determines the concentration of nucleolar components inside the nucleus, which regulates the size of the nucleolus (Weber and Brangwynne, 2015). Nucleolar size closely correlates with Pol I transcription activity and ribosome biogenesis and plays a crucial role in cell growth and size control (Brangwynne, 2013; Neumüller et al., 2013; Rudra and Warner, 2004). Studies using a variety of systems have indicated that size regulation of the nucleolus via nuclear size scaling could represent a crucial mechanism that couples cell size with nuclear synthesis and growth rates (Eaton et al., 2011; Ma et al., 2016). Thus, changes in nuclear and nucleolar size scaling provide information about the cell state, especially its synthetic activities and the metabolic demands of the cell. While nuclear and nucleolar sizes are routinely used as a diagnostic indicator for a variety of disease states (Jevtić and Levy, 2014), the mechanisms that coordinate different cellular components and activities to establish and maintain specific cell sizes remain largely elusive.

Skeletal muscle fibers are one of the largest cell types and possess remarkable cell size plasticity. Individual cells develop and grow by fusion of myoblasts and can contain hundreds of nuclei distributed across the cell surface (Deng et al., 2017). Based on the limited synthetic capacity of a single nucleus and the physical limitations to cellular transport and diffusion, a long-standing hypothesis (known as myonuclear domain hypothesis) postulates that each nucleus in a muscle syncytium only supplies its immediately surrounding cytoplasm with gene products (Hall and Ralston, 1989; Pavlath et al., 1989). Accordingly, studies using different model systems have suggested that muscle nuclei are positioned to minimize transport distances throughout the cytoplasm (Bruusgaard et al., 2003; Manhart et al., 2018). Across species, the number of myonuclei is



considered the main determinant of overall muscle cell size; however, nuclear numbers vary depending on factors such as muscle fiber type, activity, or age, indicating that the average size of the cytoplasmic domain associated with each nucleus is highly variable (Van der Meer et al., 2011). Further, differences exist within a muscle fiber in nuclear density and/or gene expression, particularly in nuclei adjacent to specialized sub-cellular structures such as muscle attachment sites (myotendinous junctions, MTJs) and the motoneuron synapse (neuromuscular junction, NMJ) (Bruusgaard et al., 2003; Rosser and Bandman, 2003). While this suggests that muscle nuclei can adjust their synthetic activity dependent on cell size and functional demands (Gundersen, 2016; Murach et al., 2018a), it is still not clear how the contribution of individual nuclei to cell size is coordinated in a shared cytoplasmic space and whether nuclear size scaling plays a role in regulating muscle fiber size.

Diseases of the skeletal musculature are commonly associated with changes in nuclear positioning, nuclear sizes, and nuclear activities (Folker and Baylies, 2013; Malfatti and Romero, 2017; Schreiber and Kennedy, 2013), but how different muscle phenotypes result in reduced muscle function remains poorly understood. The size and the complexity of muscle tissue in vertebrates impose technical challenges that limit studies on fiber size and intracellular organization to tissue cross-sections or *in vitro* approaches. To provide a more comprehensive understanding of nuclear scaling relationships and the intrinsic regulation of cell size in multinucleated muscle fibers, we have developed a *Drosophila in vivo* system to quantify cell and nuclear parameters in fully differentiated muscle cells, genetically manipulate individual cellular components, and evaluate muscle function. This system allowed us to analyze nuclear scaling relationships on a global level (scaling of the cumulative nuclear content with total cell size) and a local level (scaling of individual nuclei with their surrounding cytoplasmic domain) and identify possible mechanisms of nuclear coordination and compensation within individual muscle fibers.

RESULTS

Drosophila Larval Body Wall Muscles Allow for 2D Quantification of Cell and Nuclear Sizes

The body wall musculature of the *Drosophila* larva is a well-established system to investigate fundamental aspects of muscle cell biology *in vivo* (Demontis et al., 2013; Deng et al., 2017; Keshishian et al., 2003; Piccirillo et al., 2014). The musculature comprises 30 different muscles, which are arranged in the same stereotyped pattern in every abdominal hemisegment (Schulman et al., 2015). Each of these glycolytic muscles consists of only one multinucleated cell with distinct size, shape, and attachment sites and is easily accessible in live or dissected preparations (Dobi et al., 2015). Here, we focused on two muscles, ventral longitudinal (VL) muscles VL3 and VL4 (also known as muscles 6 and 7), which are flat rectangular cells with disc-shaped nuclei located on only one cell surface (Figures 1A and 1B). We compared 2D and 3D quantification of cell and nuclear sizes and found that volumes and areas are proportional because of the minimal and very consistent depth of VL muscle cells and nuclei (Figures 1C–1E, S1A, and S1B). Thus, this sys-

tem allows for accurate quantification of the size of whole muscle cells and their nuclei on z-projections of confocal stacks.

To assess the full range of VL muscle sizes at the end of larval development, we used carefully staged third instar larvae from three genetic control backgrounds (see STAR Methods) and quantified VL3 and VL4 muscles at different positions along the anterior-posterior axis of each larva (abdominal hemisegments 2–6). On average, VL3 muscles were 65% bigger than VL4 muscles, with comparable sizes across individual larvae and genotypes (mean VL3, 39,767 μm^2 ; 15 nuclei; mean VL4, 25,633 μm^2 ; 10 nuclei; Figures 1F and 1G). Within each larva, VL3 muscle sizes and the cumulative area of the nuclei within each cell were significantly bigger in the anterior hemisegments 2–4 and approximated the size of VL4 muscles in more posterior hemisegments (Figures 1H, 1I, and S1C). In contrast, VL4 cell and cumulative nuclear size were consistent along the anterior-posterior axis of the larvae (Figures 1H and S1C). In both VL muscles, the average number of nuclei per cell decreased from anterior to posterior (Figure S1C). Together, VL3 and VL4 muscles provided a significantly different, but overlapping, range of cell sizes and nuclear numbers. The different relationships of cell-size parameters and nuclear number along the larval body axis further indicated that the number of nuclei may not be the best indicator for muscle cell size in VL muscle fibers.

To further validate our dataset, we performed unsupervised cluster analysis using the following parameters: cell area, cell shape (aspect ratio: length/width), cell position (abdominal hemisegment number), number of nuclei, and cumulative nuclear area. Clustering divided the data into two groups that did not show any bias for individual larvae, genotypes, or experimental replicates (Figure S1D) but clearly corresponded to VL3 and VL4 muscles (Figure 1J). These analyses confirmed that VL3 and VL4 muscles were comparable across larvae and genotypes but inherently different when compared to each other.

Muscle Nuclei Collectively Establish Precise Global Scaling with Cell Size

To achieve a comprehensive characterization of nuclear scaling with regard to the size of multinucleated muscle fibers (*global* nuclear scaling), we took advantage of the natural variation of cell size parameters that we observed in wild-type VL muscles. In addition to cell areas and nuclear numbers, we quantified the cumulative nuclear DNA content (ploidy), the cumulative area of all nuclei, and the cumulative area of all nucleoli within each cell (Figures 2A–2G). All parameters showed linear scaling with cell size across VL muscle types, however, with different linear fits (Figures 2H–2K). During *Drosophila* development, fusion of diploid embryonic myoblasts initially sets the number of nuclei per muscle fiber. Subsequently, endoreplication increases the DNA content within each nucleus to promote muscle growth in the larva (Demontis and Perrimon, 2009). Nuclear numbers ranged from 9 to 21 in VL3 and from 6 to 13 in VL4, with a considerable variation in cell sizes for every given number of nuclei (Figure 2H; correlation coefficient $R = 0.74$). We independently assessed the DNA content in VL muscles by calculating ploidy numbers in muscle nuclei based on Hoechst fluorescence intensities in diploid adult muscle progenitor cells (AMPs; Figures 2B, 2D–2G, S2A, and S2B). On average, VL3 muscles contained a total of 614 ± 153 copies, and VL4 muscles contained a total

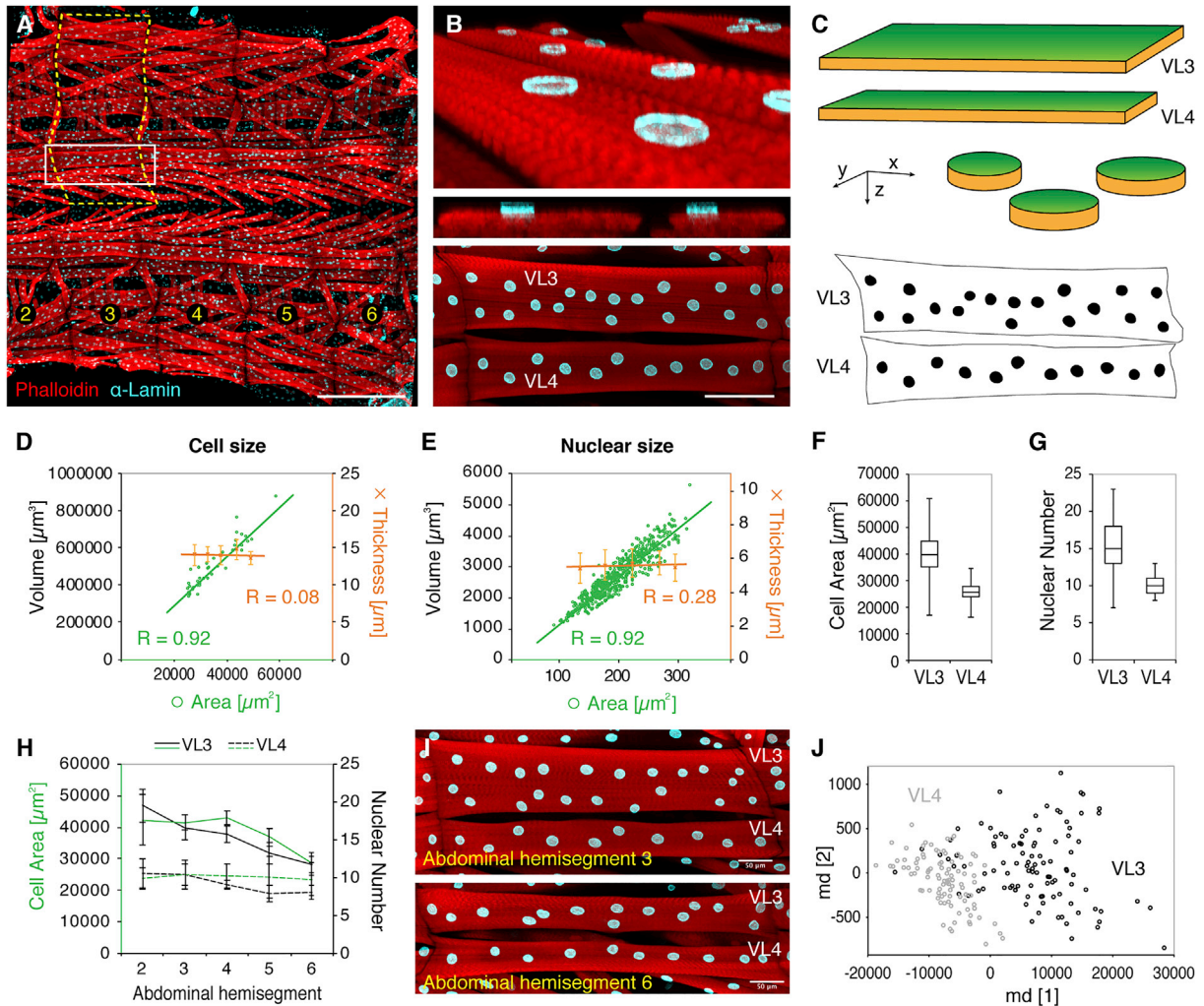


Figure 1. Quantification of Cell and Nuclear Sizes in *Drosophila* Larval Body Wall Muscles

(A) Third instar *Drosophila* larval preparation showing skeletal muscles (red, phalloidin) and nuclei (cyan, α -lamin) in bilateral abdominal hemisegments 2–6; anterior, left. Dashed line indicates one abdominal hemisegment; white box indicates ventral longitudinal (VL) muscles 3 and 4.

(B) 3D rendering (top), optical cross-section (middle), and flattened confocal z stack (bottom) of VL3 and VL4 muscles.

(C) Schematics of the geometric shapes of VL muscle cells (top) and nuclei (middle). Green areas are quantified after z-projection of confocal stacks. Bottom, binary image of VL muscles and nuclei shown in Figure 1B.

(D and E) Scatterplots comparing volume and thickness (orange) measurements with the area (green) of individual VL muscle cells (D) and nuclei (E). Linear regression curves and correlation coefficients (R) are indicated; error bars show SD. n (cells) = 42; n (nuclei) = 572.

(F and G) Median VL3 and VL4 cell areas (F) and nuclear numbers (G). Boxes, 25/75 percentiles; whiskers, min/max values. $n_{VL3} = 102$; $n_{VL4} = 97$. $p < 0.0001$ (Student's t test).

(H) VL3 (solid lines) and VL4 (dashed lines) muscle area (green) and nuclear number (black) plotted against the corresponding abdominal hemisegment of the larvae. Lines represent mean values; error bars show SD. $n_{VL3} = 102$; $n_{VL4} = 97$.

(I) VL3 and VL4 muscles from different hemisegments within the same larva.

(J) Unsupervised multidimensional cluster analysis of VL muscles from 3 different genetic control backgrounds (w^{1118} , *Dmef2-GAL4;UAS-2xEGFP*, and *Dmef2-GAL4;UAS-GFP RNAi*; two experimental replicates each) using the following parameters: cell size, cell shape (aspect ratio), nuclear number, total nuclear area, axis level (abdominal hemisegment number). VL3 (black) and VL4 (gray) muscles form separate clusters with little overlap. See also Figure S1A. $n_{VL3} = 102$; $n_{VL4} = 97$.

Scale bars, 500 μm (A), 100 μm (B), and 50 μm (I).

of 386 ± 96 copies of DNA. Notably, cells with the same number of nuclei contained different amounts of cumulative DNA content, resulting in improved linear scaling with cell area (Figure 2I; $R = 0.86$). Compared to DNA content, the cumulative area of all nucleoli and nuclei showed further improved scaling with VL cell

size (Figures 2J and 2K; $R = 0.88$ and $R = 0.90$, respectively). Plotted on a log scale, cumulative nucleolar, cumulative nuclear, and cell areas showed a linear scaling relationship (Figure S2C). Similar to DNA content, cells with the same number of nuclei established widely different cumulative nucleolar and nuclear

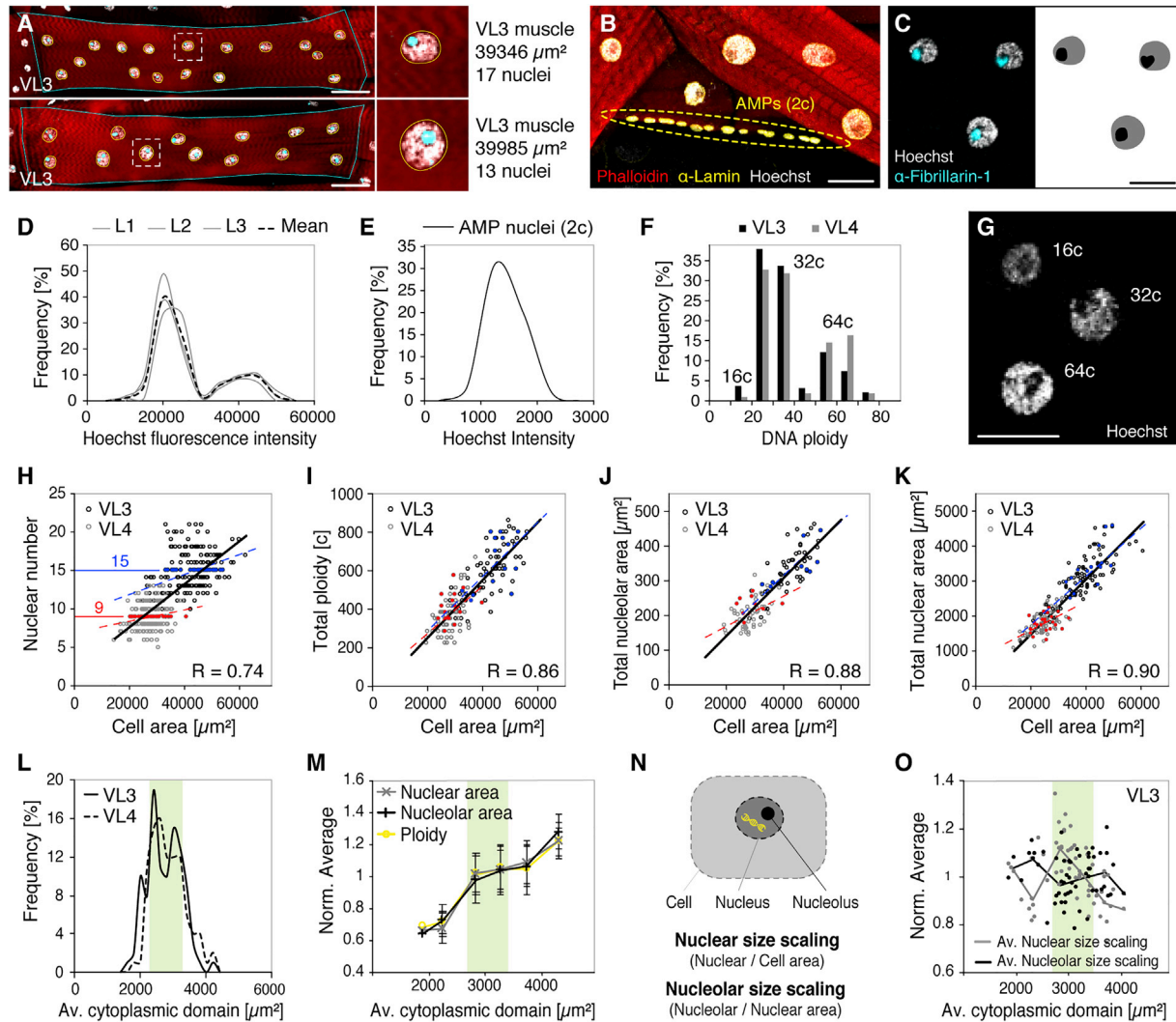


Figure 2. Muscle Nuclei Establish Precise Global Scaling with Cell Size

(A) VL3 muscles with similar areas but differences in nuclear number. Muscle cells (phalloidin, red), nuclei (Hoechst, gray), and nucleoli (α -Fibrillarlin, cyan). Boxes highlight one nucleus per cell (right); nuclear size, DNA content, and nucleolar size are increased in the cell containing fewer nuclei (bottom).

(B) Staining of DNA (Hoechst, gray) in diploid (2C) adult muscle progenitors (AMPs, dashed oval) and polyploid VL muscle nuclei. Red, phalloidin; yellow, nucleus, α -lamin.

(C) Left: labeling of nucleoli (α -Fibrillarlin, cyan) and DNA (Hoechst, gray) in VL muscle nuclei. Right: binary image for quantification of areas.

(D) Histogram of DNA (Hoechst) fluorescence intensities in individual VL muscle nuclei from 3 individual larvae (L1–L3, gray). VL nuclei per larva $n \geq 100$. Black dashed line represents mean.

(E) Histogram of Hoechst intensities in diploid (2C) AMPs. $n = 90$.

(F) Histogram of calculated DNA copy numbers (ploidy) for nuclei plotted in (A). Peaks correspond to nuclei containing 16, 32, or 64 copies (C) of DNA.

(G) Example VL nuclei containing different amounts of DNA (Hoechst). Ploidy numbers are indicated.

(H–K) Nuclear number (H; $n_{VL3} = 102$; $n_{VL4} = 97$), cumulative DNA copy number (I; $n_{VL3} = 67$; $n_{VL4} = 75$), cumulative nucleolar area (J; $n_{VL3} = 54$; $n_{VL4} = 54$), and cumulative nuclear area (K; $n_{VL3} = 102$; $n_{VL4} = 97$) plotted against muscle cell area. Bold lines and correlation coefficients (R) indicate linear scaling across VL3 (black) and VL4 (gray) muscles. Dashed lines indicate individual linear regressions for VL3 (blue) and VL4 (red) muscles. Cells with the same number of nuclei, e.g., 9 (red) and 15 (blue), achieve different cell sizes and vary in their cumulative amount of nuclear DNA, nucleolar sizes, and nuclear sizes.

(L and M) Global size parameters as in (H)–(K) normalized by the number of nuclei per cell. (L) Histogram of mean cytoplasmic domain sizes (cell area/nuclear number) in VL3 and VL4 muscles, showing similar “optimal” cytoplasmic domain size in both VL muscles (green area). (M) Mean ploidy (cumulative DNA content/nuclear number), mean nuclear area (cumulative nuclear area/nuclear number), and mean nucleolar area (cumulative nucleolar area/nuclear number) plotted against the mean cytoplasmic domain size. Green area corresponds to optimal cytoplasmic domain size as in (L). Error bars, SD.

(N) Schematic representation of nuclear size scaling and nucleolar size scaling.

(O) Nuclear size scaling and nucleolar size scaling plotted against the average size of the cytoplasmic domains within VL3 cells (for VL4, see Figure S2F). Note: the highest nuclear scaling values are associated with optimal cytoplasmic domain sizes (green area), while smaller or larger domain sizes correlate with increased nucleolar scaling and proportionally smaller nuclei.

Scale bars, 50 μm (A) and 25 μm (B, C, and G).

sizes. These data showed that VL muscle fibers establish precise global nuclear scaling relationships despite variations in the number of their nuclei. Further, this suggested a high level of coordination among the nuclei contained within a cell.

To directly compare muscle fibers with varying nuclear numbers and analyze the relationships between DNA content and nuclear and nucleolar sizes, we normalized all global parameters by the number of nuclei per cell. Thereby, we calculated the average size of the cytoplasmic domain per nucleus (cell area/nuclear number), the average DNA content per nucleus (cumulative DNA content/nuclear number), and the average size of nuclei and nucleoli (cumulative area/nuclear number). Average cytoplasmic domain sizes showed a similar distribution and range in VL3 and VL4 muscles (Figure 2L), suggesting a similar optimal cytoplasmic domain size ($\sim 3,000 \mu\text{m}^2$) per nucleus in both VL muscles. In muscles with near-optimal cytoplasmic domain sizes, average DNA content (46C), average nuclear areas ($187 \mu\text{m}^2$), and average nucleolar areas ($41 \mu\text{m}^2$) were similar. These parameters were reduced by $\sim 20\%$ – 30% in cells with smaller domain sizes and increased by $\sim 20\%$ – 30% in cells with larger domain sizes (Figure 2M). As muscle cells grow by adding DNA content, this stepwise growth pattern could reflect a stepwise increase in nuclear DNA via endoreplication.

To further investigate size scaling of nuclei and nucleoli, we determined the ratio of cumulative nuclear area per cell area (global nuclear size scaling) and the ratio of cumulative nucleolar per nuclear area (global nucleolar size scaling) (Figure 2N). On average, VL3 and VL4 muscles established significantly different global nuclear size scaling relationships, while global scaling of nucleoli to nuclei was similar in both muscles (Figures S2D and S2E). Given the function of the nucleolus in ribosome biogenesis and cell growth, proportionally larger nuclei and nucleoli in VL3 muscles indicated overall higher metabolic potential per nucleus. Strikingly, in both VL muscles, the relationship between nuclear and nucleolar scaling changed with absolute size, so that cells with near-optimal cytoplasmic domain sizes contained proportionally large nuclei and small nucleoli, while cells with smaller or larger cytoplasmic domain sizes contained proportionally small nuclei and large nucleoli (Figures 2O and S2F). This further indicated that muscle cells globally coordinate nuclear and nucleolar scaling to adjust nuclear synthetic activities dependent on DNA content and the average size of the cytoplasmic domains.

Together, these data demonstrated that a variety of nuclear parameters scale with the size of multinucleated muscle fibers; however, similar to mononucleated or diploid cells, the cumulative size of all nuclei and nucleoli give the best prediction of muscle cell size. We propose that global nuclear scaling with VL muscle size is achieved in three steps. First, the number of nuclei sets a range of possible cell sizes. Second, each cell during growth individually increases nuclear ploidies to maintain a stable scaling of cumulative of DNA content with cell size. Third, the size of nuclei and nucleoli is continuously adjusted to establish precise cell-type-specific scaling with cell size and allow for optimal cell function.

Nuclei Distribute via a Force Balance and Adjust Their Size Based on Spatial Cues

The accuracy of global nuclear scaling in multinucleated VL muscles suggested that the nuclei contained within a cell are highly

coordinated. We hypothesized that stable global scaling relationships are established via the scaling of individual nuclei with their surrounding cytoplasmic domain (*local* nuclear scaling). To test this, we determined nuclear positions within each cell based on their centroids and thus independent of their size (Figure 3A). In both VL muscles, the distances between nuclei (nearest-neighbor distances) were larger than expected for random distribution, confirming that nuclei are deliberately positioned (Figure S3A). Along the length of each fiber, nuclei were organized in rows, typically two rows in VL3 and one row in VL4 muscles (Figure 3B). However, in VL3 and VL4 muscles with the same geometric properties (cell dimensions and number of nuclei), the number and the position of rows were similar (Figure 3C), indicating that geometrical factors, rather than VL muscle type, dictate the nuclear patterns.

In *Drosophila* and mammalian muscle fibers, nuclear positioning involves microtubules and motor proteins to generate mechanical forces (Folker and Baylies, 2013; Gundersen and Worman, 2013; Roman and Gomes, 2018). In larval VL3 and VL4 muscles, microtubules grow from the nuclear envelopes and form astral arrays surrounding each nucleus (Figures 3D and S3B) (Metzger et al., 2012; Volk, 2013; Rosen et al., 2019). We hypothesized that these microtubule asters interact with each other and with the cell edges, potentially through microtubule-associated motors, and that these mechanical interactions position the nuclei (Figure 3D). We performed mathematical simulations to test whether such mechanical forces were sufficient to explain the nuclear positioning in VL3 and VL4 muscles (see STAR Methods). In brief, we assumed that the nuclei interact with each other and with the cell edges via pairwise, distance-dependent forces. We assumed that these forces are repulsive and decrease with distance. We also tested differences in the relative magnitude of inter-nuclear and nucleus-cell edge forces but kept the forces independent of nuclear sizes and positions. For each experimentally measured cell, we used the real cell dimensions and nuclear numbers and initially placed the nuclei at their measured positions. Then, applying the distance-dependent forces, we calculated their resulting positions caused by force balancing (Figure 3D). The simulated data, shown in Figures 3B and 3C, closely recapitulated the experimentally measured nuclear positioning in both VL3 and VL4 cells. The accuracy of the mathematical approximation supported that positioning mechanisms are based on microtubule-based mechanical forces and establish a cell-geometry-dependent force balance to position the nuclei in VL3 and VL4 muscles.

If nuclei are positioned via mechanical interactions yet independent of their size, we hypothesized that these nuclei sense the size of their surrounding cytoplasmic domain and adjust their own size accordingly to establish local size scaling relationships. To evaluate this hypothesis, we tested a space-sensing mechanism that predicts the size of each nucleus based on the detected amount of a hypothetical diffusible cytoplasmic molecule (Figure 3E). We assumed that signal molecules are activated or created with a constant rate and equal probability everywhere in the cell, diffused, and, upon encountering a nucleus, are taken up by the nucleus. Subsequently, each nucleus adjusts its size depending on how much signal it receives (see STAR Methods and Methods S1). Using experimentally determined cell shapes and nuclear positions, our simulations predicted nuclear areas

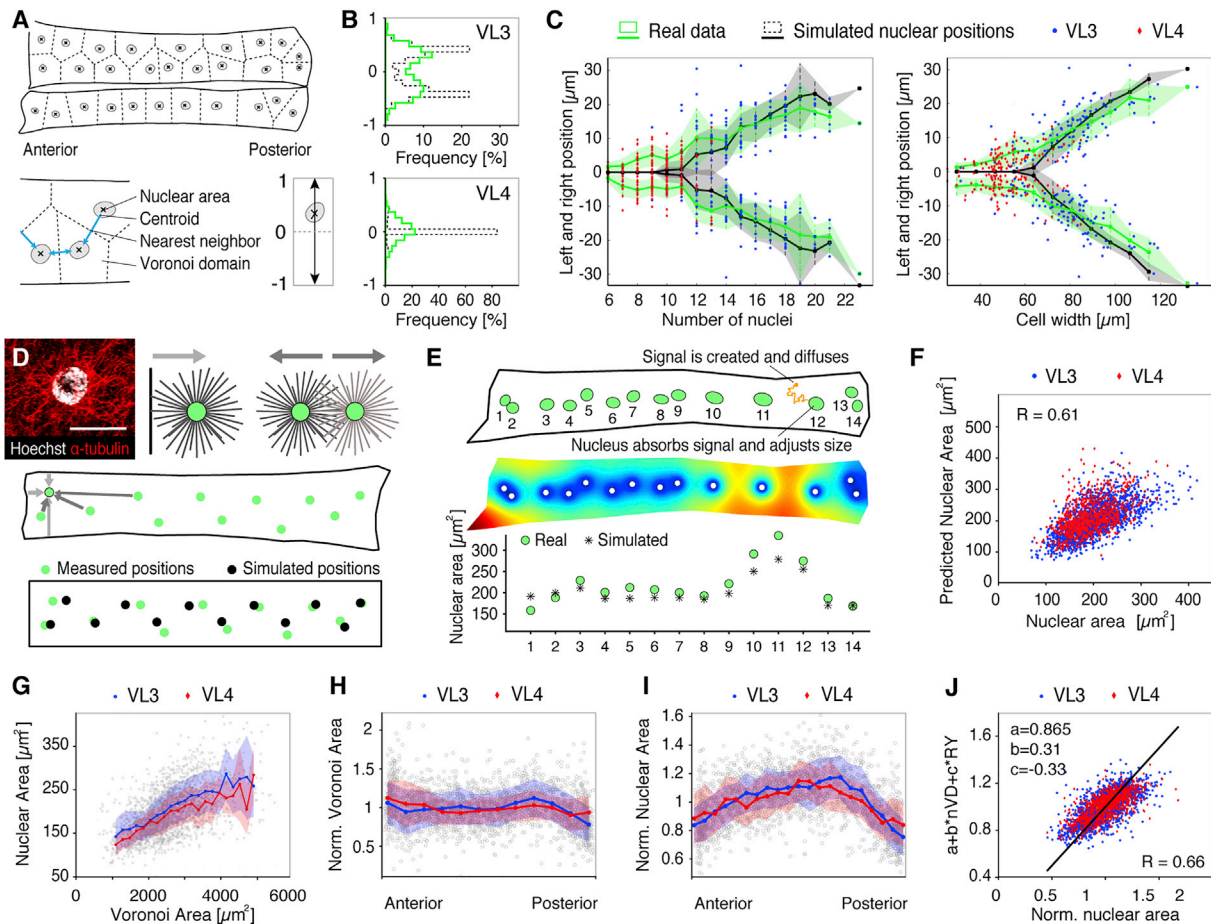


Figure 3. Nuclei Are Positioned via a Force Balance and Individually Adjust Their Sizes Based on Spatial Cues

(A) Schematic representation of VL3 and VL4 muscles and nuclei, nuclear centroids, nearest-neighbor distances (blue arrows), and cytoplasmic domain sizes (Voronoi tessellation, dashed lines).

(B) Histograms of relative nuclear positions along the short cell axis (A, bottom right). Real data (green lines) and simulated nuclear positions (dashed lines) show organization in one or two rows for each muscle type. For simulation details, see [STAR Methods](#).

(C) Nuclear positioning as a function of nuclear number (left) and cell width (right). For each cell, the average position of all nuclei to either side of the cell midline was plotted (experimental data in green; simulated data in black). Thick lines and shaded regions show means, SD; each dot represents one cell (VL3 blue; VL4, red).

(D) Simulation of nuclear positioning. Top: VL nucleus (DNA, gray) and microtubule labeling (anti- α -tubulin, red) (left) and schematic representation of the potential mechanical pushing forces between nuclei and cell edges (middle) and between neighboring nuclei (right). Lines represent microtubules, green circles represent nuclei, and arrows indicate the resulting forces. Middle: cell outline (black) and nuclear positions (green circles) of one example VL3 cell. Arrows represent forces felt by the nucleus marked with a black outline from neighboring nuclei (dark gray arrows) and cell edges (light gray arrows). Arrow width represents force strength. Bottom: for the example cell above, initial nuclear positions (measured, green circles) and final force-balanced positions (simulated, black circles) are shown. For simulation details, see [Methods S1](#). Scale bar, 25 μm .

(E) Simulation of nuclear-space sensing. Top: nuclear positions, sizes, and shapes (green discs, using fitted ellipses) of one example VL3 cell. The orange particle represents one modeled space-sensing molecule. Middle: final distribution of the space-sensing molecule as simulated for the example cell above (blue, zero concentration; red, maximal concentration). Bottom: measured and simulated nuclear areas for the example cell above. Nuclei are indexed from left to right as indicated at the top. For simulation details, see [Methods S1](#).

(F) Scatterplot showing correlation of real nuclear areas with nuclear areas predicted by simulation of local size sensing. Inset (top) shows representative simulation result; colors indicate concentration of a hypothetical cytoplasmic molecule, which is absorbed by each nucleus (white circles).

(G–J) Thick lines and shaded regions show means and SD; each dot represents one cell (VL3, blue; VL4, red). (G) Linear correlation of nuclear areas with Voronoi domain areas ($R = 0.55$; $p < 0.0001$). (H) Distribution of normalized Voronoi domain size (Voronoi area \times no. of nuclei/cell area) along the cell length. Thick lines show averages; shaded regions correspond to SD. (I) Distribution of normalized nuclear areas (nuclear area \times no. of nuclei/total nuclear area) along the cells showing largest nuclei in the cell middle. VL3 nuclei (mean \pm SD = $202 \pm 55 \mu\text{m}^2$) are larger than VL4 nuclei ($192 \pm 44 \mu\text{m}^2$). (J) Multiple linear regression showing that Voronoi area (nVD = normalized Voronoi area) and nuclear position along the long cell axis (RY = absolute relative y position, with 0 = middle and 1 = poles) give a good prediction of nuclear size ($R = 0.66$; $p < 0.0001$). Each dot represents one cell (VL3, blue; VL4, red).

Sample numbers: n (cells) = 200 (103 VL3; 97 VL4), n (nuclei) = 2,477 (1,579 VL3; 898 VL4).

very accurately, with an average relative error of less than 17% compared to the experimental data (Figure 3F). An intuitive explanation for this mechanism is that nuclei positioned farther away from their neighbors harvest the signaling molecules from the greater area and hence grow larger than their neighbors, leading to the local size regulation. Our data suggest that a local space-sensing mechanism is involved in regulating nuclear sizes within each cell.

Our space-sensing model predicted correlations between the size of individual nuclei and the size of their surrounding cytoplasmic domain. To test this *in vivo*, we used an unbiased approach to geometrically partition each cell into cytoplasmic domains based on nuclear positions (Voronoi tessellation) (Du et al., 2010; Figure 3A). In accordance with our simulations, we found a linear correlation between nuclear and Voronoi areas in both VL muscle types (Figure 3G). However, in contrast to the precise global nuclear size scaling relationships (Figure 2G; $R = 0.90$), the local correlation of nuclear size and cytoplasmic domain size was much weaker ($R = 0.55$). Closer analysis revealed that Voronoi domain areas were relatively consistent within each muscle fiber (Figure 3H), while the size of individual nuclei varied significantly (Figure 3I). Strikingly, in both VL muscles, nuclear areas showed a specific, asymmetric pattern with the biggest nuclei located close to the cell center and considerably smaller nuclei at the cell ends. This intracellular pattern of nuclear sizes was not predicted by our space-sensing model (Figure S3C), indicating that additional *regional* factors differentially affect nuclear sizes along the length of each VL muscle fiber. Multiple linear regression analyses using various cell parameters confirmed that the best prediction of nuclear size was achieved by a combination of local cytoplasmic domain area and nuclear position within the cell (Figure 3J; $R = 0.66$; $p < 0.0001$). This demonstrated that VL muscle nuclei do establish specific local size scaling with their surrounding cytoplasmic domain; however, each cell contained a heterogeneous population of nuclei with different sizes.

Together, these data suggested that VL nuclei are coordinated, via a force balance, to evenly distribute throughout the cells and establish stable global scaling relationships by adjusting their size based on local spatial parameters. In addition to the size of the cytoplasmic domain, our data predict that regional factors, which consistently vary along the length of each muscle fiber, regulate nuclear sizes within each VL muscle.

Muscle Fibers Are Composed of Domains with Distinct Nuclear Scaling Relationships

Each skeletal muscle fiber attaches to tendon cells at both cell ends (MTJs) and is innervated by a motoneuron at the NMJ. VL3 and VL4 muscles form MTJs at the anterior and posterior abdominal hemisegment boundaries and are innervated by the same motoneuron off-center, in the anterior half of the cells (Figure 4A). Strikingly, in both VL muscles, the highest local nuclear size scaling values (nuclear area/Voronoi area) correlated with the position of the NMJ (start: $29\% \pm 5\%$; end: $54\% \pm 8\%$ of cell length), while nuclei adjacent to anterior and posterior MTJs showed significantly lower values (Figures 4B and S4A). This indicated that, within each VL muscle fiber, differences in nuclear size scaling correlate with regions associated with specific cell functions during muscle contraction.

To determine whether nuclear DNA content affects local nuclear size scaling, we calculated DNA copy numbers for each VL nucleus, using established techniques (e.g., Losick et al., 2013). We identified nuclei with 16, 32, or 64 copies of DNA, which, on average, occurred at a similar frequency in VL3 and VL4 muscles (Figures 4C–4E and S2A–S2D). However, each cell established a distinct ratio of nuclear ploidy numbers in correlation with the number of nuclei and cell size, so that cells with larger cytoplasmic domain sizes contained a higher percentage of 64C nuclei. Along the cells, 16C nuclei were located adjacent to the MTJs and were absent from the NMJ region; 32C nuclei were positioned throughout the cell, and 64C nuclei were located mainly adjacent to the NMJ (Figure 4F). On average, nuclear DNA content was highest in nuclei adjacent to the NMJ in both VL muscles (Figure S4B). We compared size parameters associated with 32C and 64C nuclei: a doubling in DNA content correlated with significant increases in nuclear area ($\sim 35\%$) and cytoplasmic (Voronoi) domain area ($\sim 21\%$). Further, local nuclear size scaling (nuclear area/Voronoi area) was increased for 64C nuclei (Figure 4G). These data suggested that nuclear ploidy affects absolute size, as well as local nuclear size scaling. Nevertheless, both 32C and 64C nuclei established similar size scaling patterns along the anterior-posterior axis of the VL muscle fibers (Figure 4H), indicating that regional intracellular size scaling differences are established independent of absolute nuclear DNA content.

Variations in nuclear DNA content suggested significant local differences in nuclear synthetic activity within each VL muscle fiber. We analyzed individual nucleolar sizes as a readout for the synthetic activity of VL muscle nuclei (Figure 4I). Across all VL nuclei, absolute nucleolar areas showed a better linear correlation with nuclear areas than with Voronoi domain areas and were significantly larger in 64C than in 32C nuclei ($\sim 24\%$; Figures 4G, S4C, and S4D). Accordingly, mean nucleolar areas were largest in the anterior half of the muscle fibers and the NMJ region (Figure 4J). To independently assess nuclear synthetic activity, we analyzed labeling of H3K9ac, a conserved marker of gene activation that does not report rRNA transcription (Boros, 2012; Peng and Karpen, 2007). H3K9ac fluorescence intensities indicated that the mean number of active transcriptional start sites increased proportionally with nuclear ploidy; thus, normalizing by DNA content resulted in similar relative H3K9ac levels in 16C, 32C, and 64C nuclei (Figure 4K). Along the length of both VL muscles, H3K9ac levels showed clear regional differences and were proportionally increased in the anterior half of the cells (Figure 4L). Together, DNA content, nucleolar sizes, and H3K9ac indicated the highest nuclear activity in the anterior half of the cells, including the region of the NMJ.

We used the local scaling of nucleolar to nuclear areas to further investigate the relative contribution of individual nuclei to the total synthetic activity of each cell. In mononucleated cells with a set number of nucleolar components, nucleolar size is determined in a concentration-dependent manner by the relative size of the nucleus within the cell (Brangwynne, 2013; Ma et al., 2016; Uppaluri et al., 2016; Weber and Brangwynne, 2015). If muscle nuclei contribute to a shared pool of nucleolar components, small nuclei containing less DNA would import a proportionally increased number of nucleolar components and form proportionally larger nucleoli. Indeed, local nucleolar size scaling

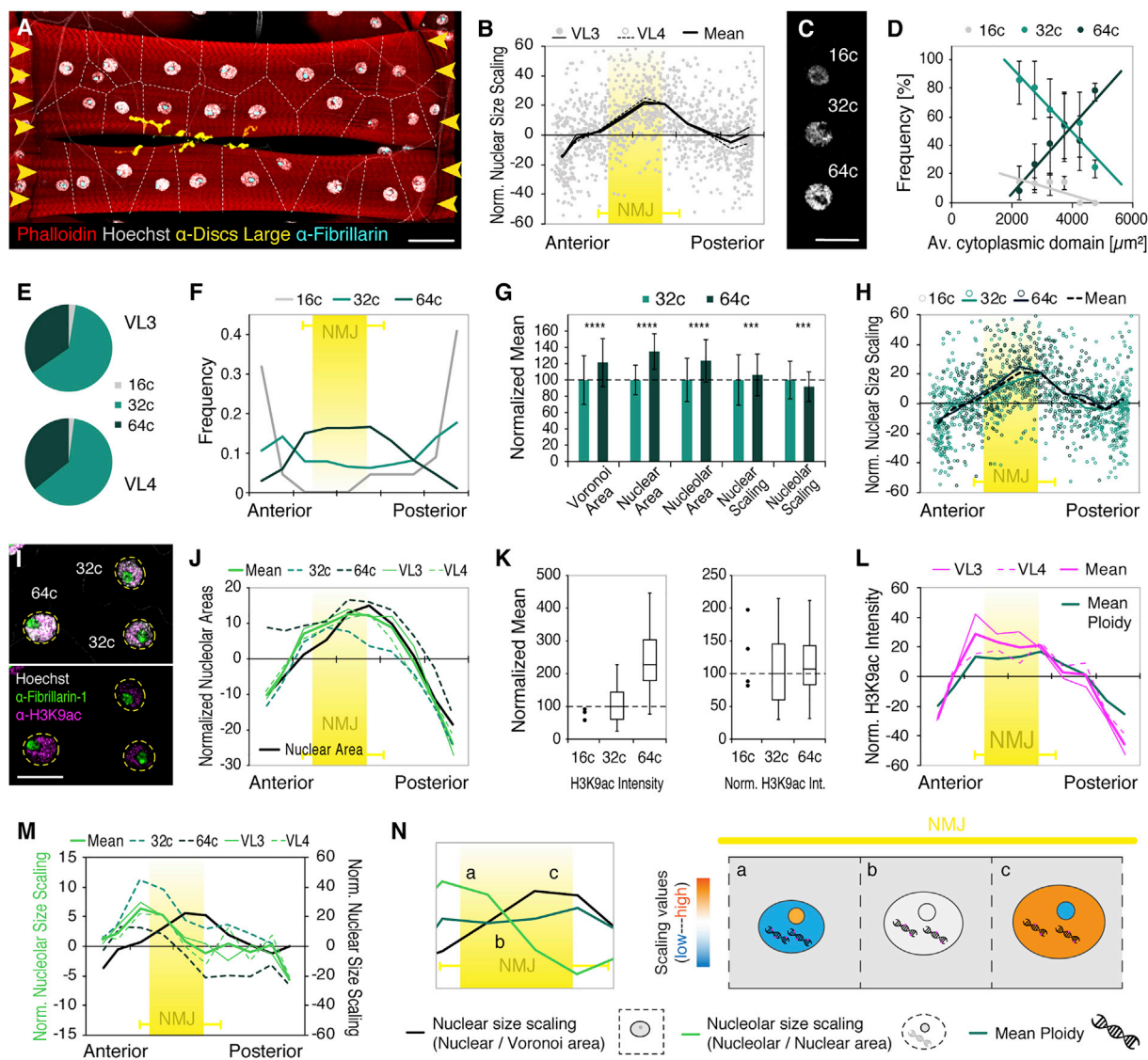


Figure 4. Local Nuclear Size Scaling and Synthetic Activity Are Inversely Correlated

(A) Positions of NMJ (α -discs large, yellow) and MTJs (yellow arrowheads) in VL3 and VL4 muscles. Muscle, red, phalloidin; nuclei, white, Hoechst; nucleolus, cyan, α -Fibrillarin.

(B) Scatterplot showing distribution of normalized local nuclear size scaling (ratio of nuclear area to Voronoi domain) along the length of VL muscle fibers ($n_{VL3} = 57$; $n_{VL4} = 61$ muscles). Highest values correlate with mean position of the NMJ (yellow; start: $29.03\% \pm 4.48\%$; end: $53.74\% \pm 7.88\%$ of cell length; $n_{VL3} = 24$; $n_{VL4} = 24$). Error bars, SD.

(C) VL muscle nuclei containing 16, 32, or 64 copies (C) of DNA. See also Figures S2A–S2D.

(D) Frequency of 16C, 32C, and 64C nuclei as a function of mean Voronoi domain size. The ratio of nuclear ploidy numbers in individual cells depends on nuclear number and cell size. Error bars, SD

(E) Pie charts showing similar ratio of nuclear ploidy numbers in VL3 and VL4 muscles.

(F) Histogram of nuclear ploidy numbers along the long cell axis (anterior, left; posterior, right). NMJ region noted by yellow box as in (B).

(G) Bar graph (mean \pm SD) comparing absolute size of Voronoi domain ($p < 0.0001$), nuclear area ($p < 0.0001$) and nucleolar area ($p < 0.0001$), and size scaling of nuclei ($p = 0.0009$) and nucleoli ($p < 0.0001$) in nuclei with 32 and 64 copies of nuclear DNA. Means for 32C nuclei were set to 100%.

(H) Nuclear size scaling (nuclear per Voronoi area) along the length of VL muscle fibers. DNA copy number for each nucleus plotted. NMJ position is indicated in yellow error bars as in (B).

(I) Representative images showing nucleoli (Fibrillarin-1, green), H3K9ac (magenta), and DNA (Hoechst, gray) in polyploid VL nuclei.

(J) Normalized nucleolar areas plotted against cell length. Mean values for nuclei with 32C and 64C and VL3 and VL4 muscles are indicated. Black line shows normalized DNA content for reference. NMJ region (yellow box) as in (B).

(K) Boxplots (median; 25/75 percentile; min/max values) showing proportional increase of H3K9ac with DNA content and thus similar relative values per nucleus, independent of absolute DNA content.

(L) Normalized H3K9ac intensity measurements plotted against cell length. Mean values for VL3 and VL4 muscles are indicated. Dark green line shows normalized DNA content for reference. NMJ region (yellow box) as in (B).

(legend continued on next page)

was significantly increased in 32C nuclei, indicating proportionally higher nuclear synthetic activity in nuclei containing less DNA (Figure 4G). Along the anterior-posterior axis of the cells, the pattern of nucleolar size scaling showed specific regional differences that were recapitulated by both 32C and 64C nuclei and similar in VL3 and VL4 muscles (Figure 4M). These results indicated that nucleolar size scaling (nucleolar area divided by nuclear area) was established independent of absolute size parameters. Intriguingly, the intracellular pattern of nucleolar size scaling was inverted compared to nuclear size scaling, so that nucleolar size scaling was lower in proportionally large nuclei and higher in proportionally small nuclei (Figure 4N). These data suggested that within each muscle cell, size scaling of nucleoli could coordinate nuclear synthetic activities to compensate for differences in nuclear DNA content as well as for differences in local nuclear size scaling.

Together, these data showed that each muscle fiber consists of domains with distinct nuclear scaling relationships. Scaling of nuclear size, DNA content, and synthetic activity exhibit different, asymmetric patterns along the length of both VL muscle fibers and correlate with regions associated with different cell functions during muscle contraction. We propose inverse size scaling of the nucleolus as a possible mechanism for muscle cells to allow for local differences in DNA content and nuclear sizes while maintaining similar cytoplasmic domain sizes along each muscle fiber and stable global cell size regulation.

Nuclear Compensation and Functional Consequences

Our analyses suggested that DNA content affects the absolute size of cells, nuclei, and nucleoli, while nuclear positioning and local size scaling are regulated independent of nuclear ploidy. To test our assumptions and investigate the robustness of nuclear scaling and cell function, we genetically manipulated the DNA content in the larval musculature. We knocked down a component of the DNA replication machinery (*Dmef2* > *ctd1(dup)RNAi*) to reduce the amount of endoreplication (Whitaker et al., 2000) and overexpressed a regulator of cell-cycle progression (*Dmef2* > *dMyc*) to promote endoreplication specifically in muscle during larval growth (Pierce et al., 2004). These manipulations resulted in significant differences in nuclear DNA content: *Cdt(Dup)* knockdown (KD) reduced nuclear ploidy numbers by one round of endoreplication (8C, 3%; 16C, 83%; 32C, 14%), whereas *Myc* overexpression (OE) increased nuclear ploidies by approximately one round of endoreplication (32C, 6%; 64C, 38%; 128C, 55%; 256C, 1%) (Figures 5A and 5C). *Cdt1(Dup)KD* muscles were only 10% smaller, and *MycOE* muscles had similar cell sizes compared to controls; however, larval locomotion was significantly reduced in both genotypes (Figures 5B and 5D). This indicated that our tissue-specific manipulations of DNA content negatively affected muscle function but did not override the systemic demands for a specific mus-

cle size. These manipulations thus provided an opportunity to investigate nuclear adaptations to changes in intracellular scaling relationships.

Analysis of global nuclear scaling relationships (cumulative nuclear parameter/cell size) showed that *Cdt1(Dup)KD* and *MycOE* did not affect the number of VL nuclei; thus, scaling of nuclear number with cell size was similar to control muscles (Figures 5E and 5F). Despite changes in absolute parameter values, precise linear scaling of cumulative DNA content and nuclear and nucleolar areas with VL cell areas was also maintained in *Cdt1(Dup)KD* and *MycOE* backgrounds (Figures 5G–5I). These data indicated that intracellular scaling mechanisms and the coordination of nuclei within each cell were not disrupted and were independent of absolute size parameters.

In accordance with our simulations of nuclear positioning in control cells, *Cdt1(Dup)KD* and *MycOE* nuclei were evenly positioned despite different nuclear sizes and DNA content (Figures 6A–6C). Further, in both genotypes, DNA ploidy numbers and nuclear sizes were smallest adjacent to the MTJs and increased toward the cell center and NMJ (Figures 6D and S5A). Strikingly, the normalized distribution of nuclear sizes along each cell was similar in *MycOE*, *Cdt1(Dup)KD*, and control muscles (Figure 6E), suggesting that regional patterning mechanisms within the cell were intact and regulated relative sizes rather than absolute nuclear parameters within each cell.

On average, *Cdt1(Dup)KD* resulted in a 62% reduction in total DNA content and 60% reduction in cumulative nucleolar areas, while the cumulative area of all nuclei was only 25% smaller than in control cells (Figures 5 and S5B–S5D). Thus, *Cdt1(Dup)KD* nuclei increased their size relative to DNA content. However, small nucleolar sizes suggested that synthetic activity was not upregulated under these conditions (e.g., no compensation). Instead, cumulative nucleolar areas maintained a linear correlation with total DNA content (Figure 6F), suggesting that the amount of nuclear DNA limits maximal nucleolar sizes within each muscle cell. In accordance with a low number of nucleolar components and proportionally increased nuclear sizes, nucleolar size scaling (nucleolar size/nuclear size) was significantly decreased in *Cdt1(Dup)KD* nuclei compared to control (Figure 6G). Despite lower global size scaling values in *Cdt1(Dup)KD* muscles, the regional patterns of local nuclear and nucleolar size scaling within the cells were similar to control (Figure 6I). These data indicated that local size scaling mechanisms were intact in *Cdt1(Dup)KD* muscles. Limitations to the synthetic machinery could reduce muscle function and growth by not meeting the metabolic demands of the muscle cells.

MycOE resulted in a doubling in cumulative DNA content, a 4-fold increase in cumulative nucleolar area, and a doubling in cumulative nuclear area (Figures 5 and S5B–S5D). In addition to promoting the replication of nuclear DNA, *MycOE* has been shown to promote rRNA synthesis, ribosome biogenesis, and

(M) Normalized nucleolar size scaling plotted against cell length. Mean values for nuclei with 32C and 64C and VL3 and VL4 muscles are indicated. NMJ region (yellow box) and normalized nuclear size scaling (black line) as in (B).

(N) Schematic highlighting the inverse relationship of nuclear and nucleolar size scaling (as in M) at constant DNA content (see L) at the NMJ. Lower case letters (a, b, c; graph, left) reflect areas from which representative nuclei and nucleolar scaling relationships are depicted in drawing (a, b, c; right).

Scale bars: 50 μm (A) and 25 μm (C and I).

Sample numbers: $n = 1,286$ nuclei (B, H, J, M, and N); $n = 950$ nuclei (D–G, K, and L).

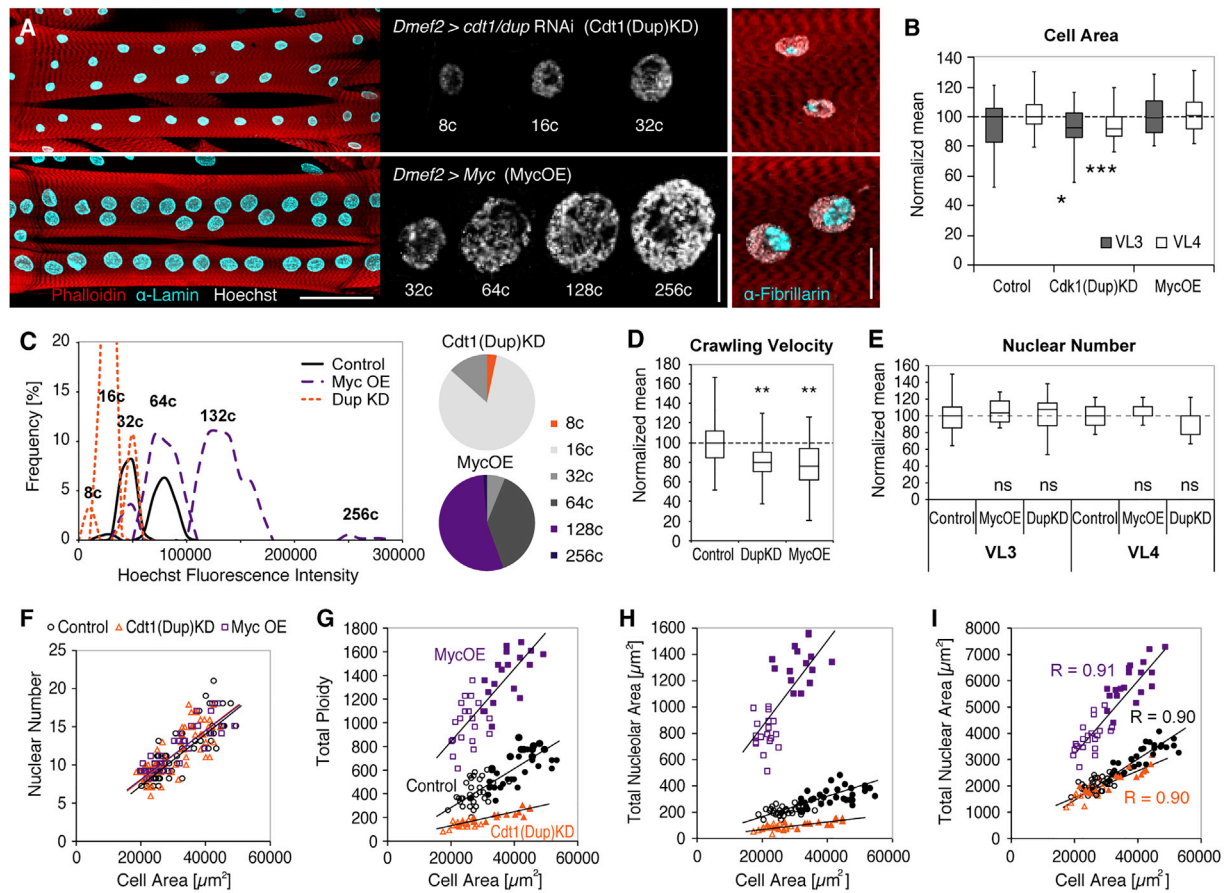


Figure 5. Muscle-Specific Increase and Decrease in Nuclear DNA Content

(A) VL3 and VL4 with muscle-specific knockdown of Cdt1(Dup) (top) and overexpression of Myc (bottom). For representative control image, see Figure 1B. Changes in nuclear DNA content (Hoechst, gray) and nucleolar sizes (α -Fibrillarlin, cyan) are shown in panels in the middle and on the right, respectively. Muscle, phalloidin, red; nuclei, α -lamin, cyan (left panel). Scale bars, 100 μ m (left), 25 μ m (middle, right).

(B) Boxplot showing median VL3 and VL4 cell areas in Cdt1(Dup)KD, MycOE, and control larvae (boxes, 25/75 percentiles; whiskers, min/max values). p values and asterisks indicate Student's t test results: Cdt1(Dup)KD, $p_{VL3} = 0.0268$; $p_{VL4} = 0.0002$; MycOE, $p_{VL3} = 0.9959$; $p_{VL4} = 0.3720$.

(C) Left: histogram of DNA (Hoechst) fluorescence intensities showing decreased nuclear DNA content in Cdt1(Dup)KD (orange) and DNA increased DNA content in MycOE muscles (purple). Right: pie charts of nuclear ploidy in Cdt1(Dup)KD and MycOE muscles. Ploidy classes not found in control muscles are highlighted in orange (8C; Cdt1(Dup)KD) and purple (128C, 256C; MycOE).

(D and E) Boxplots (whisker, min/max values; boxes, 25/75 percentiles) comparing median larval crawling velocity (D) and nuclear numbers (E) in Cdt1(Dup)KD, MycOE, and control muscles (dashed line indicates median). Student's t test results: (D) Cdt1(Dup)KD ($p = 0.0044$; $n = 24$ larvae); MycOE ($p = 0.0017$; $n = 27$ larvae).

(F–I) Scatterplots showing scaling of nuclear number (F), cumulative DNA content (G), cumulative nucleolar area (H), and cumulative nuclear area (I) across VL3 (filled symbols) and VL4 muscle types (outlined symbols) in Cdt1(Dup)KD (orange), MycOE (purple), and control muscles (black).

Sample numbers: Control, $n_{VL3} = 28$, $n_{VL4} = 35$ cells; Cdt1(Dup)KD, $n_{VL3} = 39$, $n_{VL4} = 35$ cells; MycOE, $n_{VL3} = 18$, $n_{VL4} = 19$ cells (all except D).

nucleolar sizes in a variety of *Drosophila* larval tissues (Grewal et al., 2005). Despite the dramatic increase in nucleolar areas, MycOE muscle nuclei maintained linear scaling of cumulative DNA content with cumulative nuclear areas compared to control cells (Figure 6H). This suggested that the ratio of DNA per nuclear area and thus chromatin compaction and mechanical properties of the nucleus might limit the range of nuclear size adjustments in dynamically contracting muscle fibers. In accordance with increased absolute nuclear sizes, local size scaling of nuclei and nucleoli was dramatically increased as shown in (Figure 6G). Further, along the anterior-posterior length of MycOE muscles, the coordination between local nuclear and

nucleolar size scaling was lost (Figure 6J), suggesting that the upregulation of the synthetic machinery in MycOE disrupted local size-sensing mechanisms.

Together, these data suggest that VL muscle nuclei regulate their size within a range set by DNA content yet differentially respond to increases and decreases in nuclear ploidy. While DNA content affects absolute nuclear sizes and synthetic activity, nuclear positioning mechanisms and functionally distinct regions within each cell determine the relative contribution of individual nuclei to cell size. These experiments highlight distinct levels of muscle size regulation in multinucleate muscle fiber (Figure 7), demonstrate the robustness of intracellular

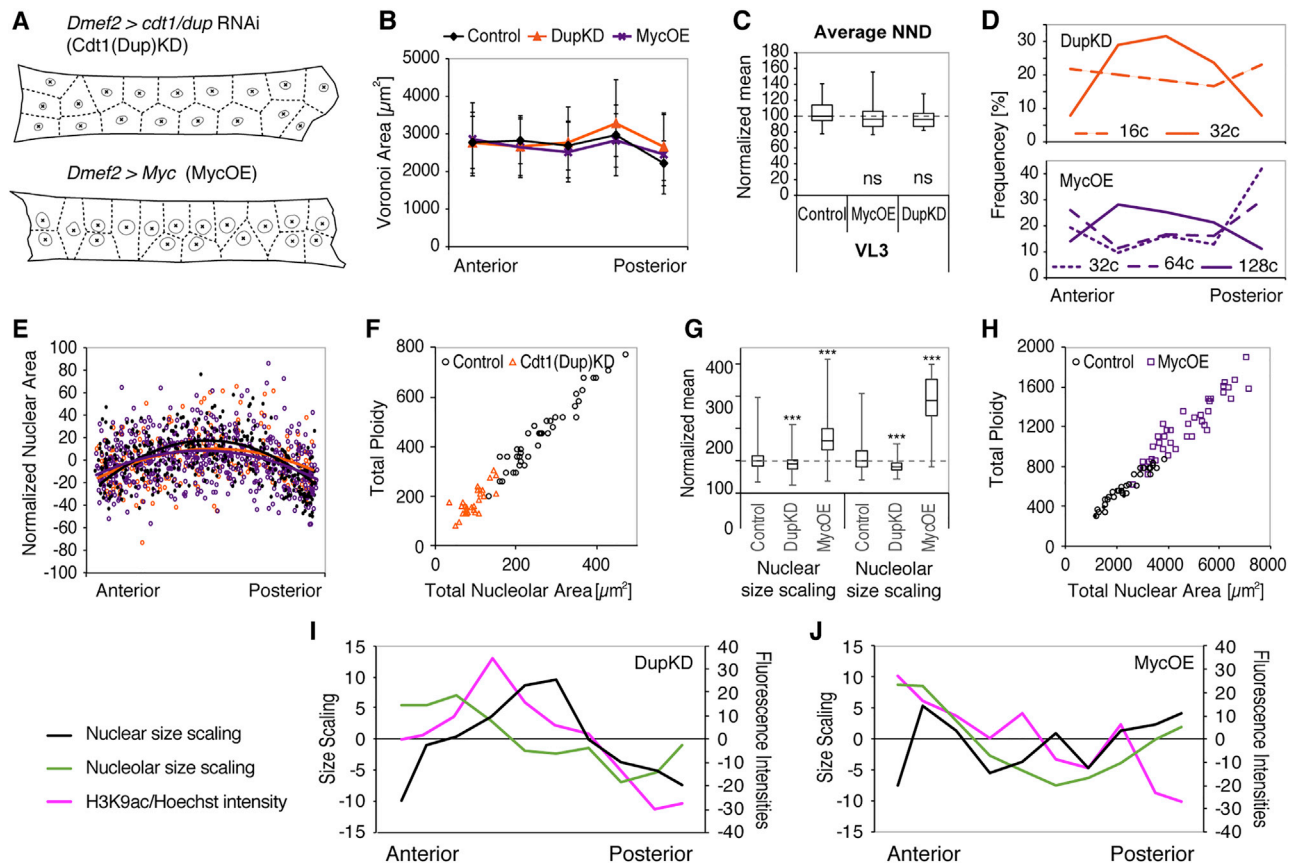


Figure 6. Intracellular Changes in Response to Manipulation of Nuclear DNA Content

(A) Schematic representation of Dup(Cdk1)KD (top) and MycOE (bottom) VL3 muscles and nuclei, including nuclear centroids, and cytoplasmic domain sizes (Voronoi tessellation, dashed lines).

(B) Voronoi domain areas along the long cell axis (mean \pm SD). Colored lines indicate genotype.

(C) Boxplot (whisker, min/max values; boxes, 25/75 percentiles) showing nearest-neighbor distance (NND) in VL3 muscles of Cdt1(Dup)KD, MycOE and control larvae. Student's t test results: $p = 0.1638$ (MycOE) and $p = 0.5448$ (Cdt1(Dup)KD).

(D) Histograms showing distribution of nuclear ploidies along the cell length of MycOE and Cdt1(Dup)KD muscles.

(E) Distribution of normalized nuclear areas along the length of each muscle fiber. Values are expressed as % deviation from average per genotype. Solid lines indicate mean. The distribution of nuclear areas in the Cdt1(Dup)KD and in MycOE is similar to control.

(F) Linear isometric scaling of cumulative nucleolar area with DNA content in Cdt1(Dup)KD muscles.

(G) Boxplot showing median nuclear and nucleolar scaling in Cdt1(Dup)KD, MycOE, and control larvae (boxes, 25/75 percentiles; whiskers, min/max values). *** indicates p values < 0.0001 for all genotypes (Student's t test).

(H) Linear isometric scaling of cumulative nuclear area with DNA content in MycOE muscles.

(I and J) Normalized nuclear and nucleolar size scaling and H3K9ac per Hoechst fluorescence intensity plotted along the length of Cdt1(Dup)KD and MycOE muscles. For wild-type patterns, see Figure 4).

Sample numbers: Control, $n_{VL3} = 28$, $n_{VL4} = 35$ cells; Cdt1(Dup)KD, $n_{VL3} = 39$, $n_{VL4} = 35$ cells; MycOE, $n_{VL3} = 18$, $n_{VL4} = 19$ cells (C–J).

organization, and stress the importance of nuclear scaling for muscle function.

DISCUSSION

Skeletal muscle fibers are large multinucleated cells with essential roles in locomotion and metabolism. Our study provides the first comprehensive analysis of nuclear scaling in whole, fully differentiated muscle fibers using a large *in vivo* dataset. We show that muscle nuclei collectively establish precise global scaling relationships with muscle cell size. However, each cell is composed of domains with distinct local scaling of DNA, nuclear size, and nuclear synthetic activities. Together, our ana-

lyses of wild-type parameters, mathematical simulations, and genetic manipulations reveal different levels of muscle size regulation (Figure 7) and implicate nuclear scaling as essential for muscle function. We suggest that the mechanisms involved in intracellular size regulation in muscle cells depend on local factors (cytoplasmic domain size), regional factors (possibly involving NMJs or MTJs), as well as global factors (muscle type).

To establish a baseline for nuclear scaling in multinucleated muscle fibers, we took advantage of the natural variation of different size parameters in *Drosophila* VL muscles. In *Drosophila* as well as in vertebrate systems, muscle fibers exhibit remarkable size plasticity, and nuclear number and DNA content are highly variable (Deng et al., 2017; Van der Meer et al., 2011).

to mononucleated cells, the inverse relationship of nuclear and nucleolar size scaling in VL muscle fibers could represent a link between absolute cell size and nuclear synthetic activity globally, as well as locally. In a shared cytoplasmic space, this mechanism would also allow for local differences in nuclear sizes and DNA content, while maintaining similar cytoplasmic domain sizes along each muscle fiber and stable global cell size regulation.

During muscle growth, increases in DNA content, in transcriptional output, and in cytoplasmic domain sizes contribute to cellular hypertrophy (e.g., this work; Kirby et al., 2016; Murach et al., 2018b; Qaisar and Larsson, 2014). While domain sizes grow continuously, DNA content increases in steps (through endoreplication in *Drosophila* or fusion in vertebrates), which requires, in theory, that nuclear activity is adjusted to compensate. Changes in cytoplasmic domain sizes have been observed in many growing vertebrate muscles (Murach et al., 2018a); however, how local nuclear synthetic activities correlated with these changes has not been analyzed in detail in whole muscle cells. Our genetic manipulations revealed which size parameters are linked and which are flexible and can compensate for changes in DNA content. Cdt1(Dup)KD nuclei increased nuclear areas despite reduced DNA content and smaller nucleoli; these data suggest changes in nuclear organization, such as chromatin organization, to overcome limitations to the synthetic machinery. MycOE muscle nuclei, in contrast, maintained the ratio of DNA per nuclear area. However, these nuclei lost cumulative nuclear size scaling with cell size (that is, smaller muscle cells than would be predicted) as well as the local coordination of nuclear and nucleolar size scaling. Overall, our data also revealed a surprising dominance of systemic size regulators, such as growth factors (Demontis and Perrimon, 2009), to fulfill the requirements for a specific muscle size. As a consequence, different intracellular phenotypes (different local scaling along the fiber) developed. *Drosophila* larvae allow for easy, muscle-specific manipulations and readouts of muscle function, which open the door for future studies linking specific muscle phenotypes to pathways of intracellular size regulation and to functional consequences.

While using *Drosophila* larval VL muscles allowed us to perform a relatively straightforward 2D quantification of muscle cell sizes and nuclear content, most vertebrate muscle fibers are cylindrical in shape with nuclei positioned along the entire fiber at the cell periphery. In addition, *Drosophila* larval muscle nuclei undergo endoreplication to increase DNA content during muscle growth, while in mice, increasing domain sizes during muscle hypertrophy can trigger increases in DNA content via cell fusion (Murach et al., 2018a; Qaisar and Larsson, 2014). Despite these differences, vertebrate and *Drosophila* muscles share many structural and functional similarities, which makes our study a suitable framework for understanding size control in different muscle systems. Further, the presence of increased nuclear DNA content has been shown in many differentiated cell types as common mechanisms to achieve large cell sizes (Orr-Weaver, 2015), making it worth testing whether vertebrate muscle nuclei actually maintain a diploid (2C) state. While the molecular mechanisms of intracellular size regulation in muscle fibers await further investigation, our study represents an impor-

tant step toward optimizing the quantification of muscle cell size and understanding the complex mechanisms of size regulation in multinucleated cells. In this regard, our data should also inform size regulation in other multinucleated cell types such as trophoblasts and osteoclasts and affect our thinking on therapies aimed at affecting muscle growth, homeostasis, and regeneration. Ultimately, identifying the regulatory network that coordinates intracellular size regulation in multinucleated muscle fibers will reveal how disruption of sub-cellular organization results in muscle disease and reduced muscle function.

STAR★METHODS

Detailed methods are provided in the online version of this paper and include the following:

- KEY RESOURCES TABLE
- CONTACT FOR REAGENT AND RESOURCE SHARING
- EXPERIMENTAL MODEL AND SUBJECT DETAILS
 - Fly Stocks and Staging
- METHOD DETAILS
 - Dissections, Labeling and Confocal Imaging
 - Image Processing and Measurements
 - Simulation of Random Nuclear Positioning
 - Simulation of Nuclear Positioning
 - Simulation of Space-Sensing
 - Larval Locomotion Assay
- QUANTIFICATION AND STATISTICAL ANALYSIS
 - Unsupervised Multidimensional Cluster Analysis
 - Multiple Linear Regression Analysis

SUPPLEMENTAL INFORMATION

Supplemental Information can be found with this article online at <https://doi.org/10.1016/j.devcel.2019.02.020>.

ACKNOWLEDGMENTS

We would like to thank T. Orr-Weaver, N. Perrimon, and the Bloomington Stock Center for flies; members of the Baylies Lab for helpful discussion, particularly M. Azevedo for critical reading of the manuscript; and R. Khanin in the MSKCC Bioinformatics core for the PCA analysis. This work was supported by the NIH (GM121971, AR068128) to M.K.B. and National Cancer Institute (P30 CA 008748) core grant to MSKCC. The funders had no role in the study design, data collection and analysis, decision to publish, or preparation of the manuscript.

AUTHOR CONTRIBUTIONS

S.E.W., M.K.B., A.Manhart., and A.Mogilner. conceived the experiments; S.E.W. and A.Manhart. carried them out. S.E.W. and A.Manhart., with input from A.M. and M.K.B., designed and carried out the data analysis. A.B. and S.E.W. automated the larval data analysis. A.B. performed volume analysis. S.E.W., A.Manhart., A.Mogilner., and M.K.B. prepared the manuscript.

DECLARATION OF INTERESTS

The authors declare no competing interests.

Received: June 15, 2018
 Revised: November 28, 2018
 Accepted: February 22, 2019
 Published: March 21, 2019

REFERENCES

- Amodeo, A.A., and Skotheim, J.M. (2016). Cell-size control. *Cold Spring Harb. Perspect. Biol.* 8, a019083.
- Boros, I.M. (2012). Histone modification in *Drosophila*. *Brief. Funct. Genomics* 11, 319–331.
- Boulan, L., Milán, M., and Léopold, P. (2015). The systemic control of growth. *Cold Spring Harb. Perspect. Biol.* 7, a019117–a019130.
- Brangwynne, C.P. (2013). Phase transitions and size scaling of membrane-less organelles. *J. Cell Biol.* 203, 875–881.
- Bruusgaard, J.C., Liestøl, K., Ekmark, M., Kollstad, K., and Gundersen, K. (2003). Number and spatial distribution of nuclei in the muscle fibres of normal mice studied in vivo. *J. Physiol. (Lond.)* 551, 467–478.
- Chan, Y.H., and Marshall, W.F. (2012). How cells know the size of their organelles. *Science* 337, 1186–1189.
- Conklin, E.G. (1912). Cell size and nuclear size. *J. Exp. Zool* 12, 1–98.
- Dej, K.J., and Spradling, A.C. (1999). The endocycle controls nurse cell polytene chromosome structure during *Drosophila* oogenesis. *Development* 126, 293–303.
- Demontis, F., and Perrimon, N. (2009). Integration of insulin receptor/Foxo signaling and dMyc activity during muscle growth regulates body size in *Drosophila*. *Development* 136, 983–993.
- Demontis, F., Piccirillo, R., Goldberg, A.L., and Perrimon, N. (2013). Mechanisms of skeletal muscle aging: insights from *Drosophila* and mammalian models. *Dis. Model Mech* 6, 1339–1352.
- Deng, S., Azevedo, M., and Baylies, M. (2017). Acting on identity: myoblast fusion and the formation of the syncytial muscle fiber. *Semin. Cell Dev. Biol.* 72, 45–55.
- Dobi, K.C., Schulman, V.K., and Baylies, M.K. (2015). Specification of the somatic musculature in *Drosophila*. *Wiley Interdiscip. Rev. Dev. Biol.* 4, 357–375.
- Du, Q., Gunzburger, M., and Ju, L. (2010). Advances in studies and applications of Centroidal Voronoi tessellations. *NM-TMA* 3, 119–142.
- Eaton, M.L., Prinz, J.A., MacAlpine, H.K., Tretyakov, G., Kharchenko, P.V., and MacAlpine, D.M. (2011). Chromatin signatures of the *Drosophila* replication program. *Genome Res.* 21, 164–174.
- Figeac, N., Jagla, T., Aradhya, R., Da Ponte, J.P., and Jagla, K. (2010). *Drosophila* adult muscle precursors form a network of interconnected cells and are specified by the rhomboid-triggered EGF pathway. *Development* 137, 1965–1973.
- Folker, E.S., and Baylies, M.K. (2013). Nuclear positioning in muscle development and disease. *Front. Physiol.* 4, 363.
- Frawley, L.E., and Orr-Weaver, T.L. (2015). Polyploidy. *Curr. Biol.* 25, R353–R358.
- Ganesan, S., Karr, J.E., and Featherstone, D.E. (2011). *Drosophila* glutamate receptor mRNA expression and mRNP particles. *RNA Biol.* 8, 771–781.
- Gillooly, J.F., Hein, A., and Damiani, R. (2015). Nuclear DNA content varies with cell size across human cell types. *Cold Spring Harb. Perspect. Biol.* 7, a019091.
- Ginzberg, M.B., Kafri, R., and Kirschner, M. (2015). On being the right (cell) size. *Science* 348, 1245075.
- Grewal, S.S., Li, L., Orian, A., Eisenman, R.N., and Edgar, B.A. (2005). Myc-dependent regulation of ribosomal RNA synthesis during *Drosophila* development. *Nat. Cell Biol.* 7, 295–302.
- Gundersen, G.G., and Worman, H.J. (2013). Nuclear positioning. *Cell* 152, 1376–1389.
- Gundersen, K. (2016). Muscle memory and a new cellular model for muscle atrophy and hypertrophy. *J. Exp. Biol.* 219, 235–242.
- Keshishian, H., Broadie, K., Chiba, A., and Bate, M. (2003). The *Drosophila* neuromuscular junction: a model system for studying synaptic development and function. *Annu. Rev. Biochem.* 19, 545–575.
- Hall, Z.W., and Ralston, E. (1989). Nuclear domains in muscle cells. *Cell* 59, 771–772.
- Jevtić, P., and Levy, D.L. (2014). Mechanisms of nuclear size regulation in model systems and cancer. *Adv. Exp. Med. Biol.* 773, 537–569.
- Kirby, T.J., Patel, R.M., McClintock, T.S., Dupont-Versteegden, E.E., Peterson, C.A., and McCarthy, J.J. (2016). Myonuclear transcription is responsive to mechanical load and DNA content but uncoupled from cell size during hypertrophy. *Mol. Biol. Cell* 27, 788–798.
- Levy, D.L., and Heald, R. (2012). Mechanisms of intracellular scaling. *Annu. Rev. Cell Dev. Biol.* 28, 113–135.
- Losick, V.P., Fox, D.T., and Spradling, A.C. (2013). Polyploidization and cell fusion contribute to wound healing in the adult *Drosophila* epithelium. *Curr. Biol.* 23, 2224–2232.
- Losick, V.P., Jun, A.S., and Spradling, A.C. (2016). Wound-induced polyploidization: regulation by hippo and JNK signaling and conservation in mammals. *PLoS One* 11, e0151251.
- Ma, T.H., Lee, L.W., Lee, C.C., Yi, Y.H., Chan, S.P., Tan, B.C.-M., and Lo, S.J. (2016). Genetic control of nucleolar size: an evolutionary perspective. *Nucleus* 7, 112–120.
- Malfatti, E., and Romero, N.B. (2017). Diseases of the skeletal muscle. *Handb. Clin. Neurol* 145, 429–451.
- Manhart, A., Windner, S., Baylies, M., and Mogilner, A. (2018). Mechanical positioning of multiple nuclei in muscle cells. *PLoS Comput. Biol.* 14, e1006208.
- Merlie, J.P., and Sanes, J.R. (1985). Concentration of acetylcholine receptor mRNA in synaptic regions of adult muscle fibres. *Nature* 317, 66–68.
- Metzger, T., Gache, V., Xu, M., Cadot, B., Folker, E.S., Richardson, B.E., Gomes, E.R., and Baylies, M.K. (2012). MAP and kinesin-dependent nuclear positioning is required for skeletal muscle function. *Nature* 484, 120–124.
- Miettinen, T.P., Pessa, H.K.J., Caldez, M.J., Fuhrer, T., Diril, M.K., Sauer, U., Kaldis, P., and Björklund, M. (2014). Identification of transcriptional and metabolic programs related to mammalian cell size. *Curr. Biol.* 24, 598–608.
- Mukherjee, R.N., Chen, P., and Levy, D.L. (2016). Recent advances in understanding nuclear size and shape. *Nucleus* 7, 167–186.
- Murach, K.A., Englund, D.A., Dupont-Versteegden, E.E., McCarthy, J.J., and Peterson, C.A. (2018a). Myonuclear domain flexibility challenges rigid assumptions on satellite cell contribution to skeletal muscle fiber hypertrophy. *Front. Physiol* 9, 635.
- Murach, K.A., Fry, C.S., Kirby, T.J., Jackson, J.R., Lee, J.D., White, S.H., Dupont-Versteegden, E.E., McCarthy, J.J., and Peterson, C.A. (2018b). Starring or supporting role? Satellite cells and skeletal muscle fiber size regulation. *Physiology (Bethesda)* 33, 26–38.
- Neumüller, R.A., Gross, T., Samsonova, A.A., Vinayagam, A., Buckner, M., Founk, K., Hu, Y., Sharifpoor, S., Rosebrock, A.P., Andrews, B., et al. (2013). Conserved regulators of nucleolar size revealed by global phenotypic analyses. *Sci. Signal* 6, ra70.
- Nordman, J., Li, S., Eng, T., Macalpine, D., and Orr-Weaver, T.L. (2011). Developmental control of the DNA replication and transcription programs. *Genome Res.* 21, 175–181.
- Orr-Weaver, T.L. (2015). When bigger is better: the role of polyploidy in organogenesis. *Trends Genet.* 31, 307–315.
- Packard, M., Jokhi, V., Ding, B., Ruiz-Cañada, C., Ashley, J., and Budnik, V. (2015). Nucleus to synapse Nesprin1 railroad tracks direct synapse maturation through RNA localization. *Neuron* 86, 1015–1028.
- Pavlat, G.K., Rich, K., Webster, S.G., and Blau, H.M. (1989). Localization of muscle gene products in nuclear domains. *Nature* 337, 570–573.
- Peng, J.C., and Karpen, G.H. (2007). H3K9 Methylation and RNA interference regulate nucleolar organization and repeated DNA stability. *Nat. Cell Biol.* 9, 25–35.
- Penzo-Méndez, A.I., and Stanger, B.Z. (2015). Organ-size regulation in mammals. *Cold Spring Harb. Perspect. Biol.* 7, a019240.
- Piccirillo, R., Demontis, F., Perrimon, N., and Goldberg, A.L. (2014). Mechanisms of muscle growth and atrophy in mammals and *Drosophila*. *Dev. Dyn* 243, 201–215.

- Pierce, S.B., Yost, C., Britton, J.S., Loo, L.W.M., Flynn, E.M., Edgar, B.A., and Eisenman, R.N. (2004). dMyc is required for larval growth and endoreplication in *Drosophila*. *Development* *131*, 2317–2327.
- Qaisar, R., and Larsson, L. (2014). What determines myonuclear domain size? *Indian J. Physiol. Pharmacol.* *58*, 1–12.
- Ranganayakulu, G., Elliott, D.A., Harvey, R.P., and Olson, E.N. (1998). Divergent roles for NK-2 class homeobox genes in cardiogenesis in flies and mice. *Development* *125*, 3037–3048.
- Roman, W., and Gomes, E.R. (2018). Nuclear positioning in skeletal muscle. *Semin. Cell Dev. Biol.* *82*, 51–56.
- Rosen, J.N., Azevedo, M., Soffar, D.B., Boyko, V.P., Brendel, M.B., Schulman, V.K., and Baylies, M.K. (2019). The *Drosophila* Ninein homologue Bsg25D cooperates with Ensconsin in myonuclear positioning. *J. Cell Biol.* *218*, 524–540.
- Rosser, B.W.C., and Bandman, E. (2003). Heterogeneity of protein expression within muscle fibers. *J. Anim. Sci.* *81*, E94–E101.
- Rosser, B.W.C., Dean, M.S., and Bandman, E. (2002). Myonuclear domain size varies along the lengths of maturing skeletal muscle fibers. *Int. J. Dev. Biol.* *46*, 747–754.
- Rudra, D., and Warner, J.R. (2004). What better measure than ribosome synthesis? *Genes Dev.* *18*, 2431–2436.
- Schreiber, K.H., and Kennedy, B.K. (2013). When lamins go bad: nuclear structure and disease. *Cell* *152*, 1365–1375.
- Schulman, V.K., Dobi, K.C., and Baylies, M.K. (2015). Morphogenesis of the somatic musculature in *Drosophila melanogaster*. *Wiley Interdiscip. Rev. Dev. Biol.* *4*, 313–334.
- Sher, N., Von Stetina, J.R., Bell, G.W., Matsuura, S., Ravid, K., and Orr-Weaver, T.L. (2013). Fundamental differences in endoreplication in mammals and *Drosophila* revealed by analysis of endocycling and endomitotic cells. *Proc. Natl. Acad. Sci. USA* *110*, 9368–9373.
- Spradling, A., and Orr-Weaver, T. (1987). Regulation of DNA replication during *Drosophila* development. *Annu. Rev. Genet.* *21*, 373–403.
- Team, R.C. (2013). R: a language and environment for statistical computing. <https://www.r-project.org/>.
- Unhavaithaya, Y., and Orr-Weaver, T.L. (2012). Polyploidization of glia in neural development links tissue growth to blood-brain barrier integrity. *Genes Dev.* *26*, 31–36.
- Uppaluri, S., Weber, S.C., and Brangwynne, C.P. (2016). Hierarchical size scaling during multicellular growth and development. *Cell Rep* *17*, 345–352.
- Van der Meer, S.F.T., Jaspers, R.T., and Degens, H. (2011). Is the myonuclear domain size fixed? *J. Musculoskelet. Neuronal Interact.* *11*, 286–297.
- Volk, T. (2013). Positioning nuclei within the cytoplasm of striated muscle fiber: cooperation between microtubules and KASH proteins. *Nucleus* *4*, 18–22.
- Weber, S.C., and Brangwynne, C.P. (2015). Inverse size scaling of the nucleolus by a concentration-dependent phase transition. *Curr. Biol.* *25*, 641–646.
- Whittaker, A.J., Royzman, I., and Orr-Weaver, T.L. (2000). *Drosophila* double parked: a conserved, essential replication protein that colocalizes with the origin recognition complex and links DNA replication with mitosis and the down-regulation of S phase transcripts. *Genes Dev.* *14*, 1765–1776.
- Yi, Y.H., Ma, T.H., Lee, L.W., Chiou, P.T., Chen, P.H., Lee, C.M., Chu, Y.D., Yu, H., Hsiung, K.C., Tsai, Y.T., et al. (2015). A genetic cascade of *let-7-ncl-1-fib-1* modulates nucleolar size and rRNA pool in *Caenorhabditis elegans*. *PLoS Genet.* *11*, e1005580.

STAR★METHODS

KEY RESOURCES TABLE

REAGENT or RESOURCE	SOURCE	IDENTIFIER
Antibodies		
Mouse anti-Lamin ADL67.10	DHSB	RRID: AB_528336
Mouse anti-Fibrillarin1 MCA 38F3	EnCore	RRID: AB_2278545
Rabbit anti-H3K9ac	Active Motif	RRID: AB_2561017
Mouse anti-Discs Large 4F3	DHSB	RRID: AB_528203
Mouse anti-alpha tubulin DM1A	Sigma	RRID: AB_212802
Goat anti-mouse Alexa conjugated secondaries	Life Technologies	RRID: AB_2534069, RRID: AB_2534071, RRID: AB_2535844, RRID: AB_2535804
Experimental Models: Organisms/Strains		
<i>D. melanogaster</i> : w ¹¹¹⁸	Bloomington Drosophila Stock Center	BDSC:3605
<i>D. melanogaster</i> : Dmef2-Gal4	Ranganayakulu et al., 1998	N/A
<i>D. melanogaster</i> : UAS-2xEGFP	Bloomington Drosophila Stock Center	BDSC:6874
<i>D. melanogaster</i> : UAS-GFP RNAi	from J. Zallen (SKI)	N/A
<i>D. melanogaster</i> : UAS-dMyc	from N. Perrimon (HMS)	N/A
<i>D. melanogaster</i> : UAS-dup (double parked/Cdt1) RNAi	from T. Orr-Weaver (MIT)	N/A
Software and Algorithms		
ImageJ/Fiji	Fiji	https://fiji.sc/
GraphPad Prism	GraphPad	https://www.graphpad.com/
Excel	Microsoft	https://products.office.com/en-us/excel
Matlab	Mathworks	https://www.mathworks.com/products/matlab.html
Imaris	Bitplane	http://www.bitplane.com/imaris/imaris
R	R Foundation for Statistical Computing	https://www.r-project.org/
Cytosim	Nédélec Laboratory	http://github.com/nedelec/cytosim
Illustrator	Adobe	www.adobe.com

CONTACT FOR REAGENT AND RESOURCE SHARING

Further information and request for resources and reagents should be directed to and will be fulfilled by the Lead Contact, Mary K. Baylies (m-baylies@ski.mskcc.org).

EXPERIMENTAL MODEL AND SUBJECT DETAILS

Fly Stocks and Staging

The following *Drosophila* stocks were maintained under standard laboratory conditions (25°C) on BDSC cornmeal medium (Bloomington Drosophila Stock Center: <https://bdsc.indiana.edu/information/recipes/bloomfood.html>): w¹¹¹⁸ (Bloomington 3605), *Dmef2-GAL4* ([Ranganayakulu et al., 1998](#)), *UAS-2xEGFP* (Bloomington 6874), *UAS-GFP RNAi* (from J. Zallen, SKI), *UAS-dmyc* (from N. Perrimon), *UAS-dup (double parked/Cdt1) RNAi* (from T. Orr-Weaver). Crosses (GAL4 X UAS) were performed at 25°C on apple juice plates under 12:12 Light:Dark conditions and constant humidity. For all experiments, embryos hatched within a 2h period were selected and raised to third instar larval stage on cornmeal medium at 25°C. Staging of 3rd instar larvae was confirmed using developmental landmarks, including mouth hook and spiracle morphologies. Both male and female larvae were analyzed.

METHOD DETAILS

Dissections, Labeling and Confocal Imaging

Wandering third instar larvae were dissected, fixed in 10% formalin, and labeled as previously described ([Metzger et al., 2012](#)). Muscle cells were labeled using Alexa Fluor-conjugated phalloidin (Life Technologies). Anti-Lamin (ADL67.10, DHSB; 1:100),

anti-Fibrillar (MCA-38F3, EnCor; 1:100), anti-H3K9ac (Active Motif; 1:200), anti-discs large (4F3, DSHB; 1:200), anti-alpha tubulin (Sigma, 1:500) primary antibodies and Alexa Flour-conjugated secondary antibodies (Life Technologies; 1:200) were used to label cellular and nuclear structures. Hoechst 33342 (Invitrogen; 1 µg/ml) was used to label nuclear DNA. Whole larvae were mounted in ProlongGold (Invitrogen). VL3 and VL4 muscles in abdominal hemisegments 2-6 were imaged on a LSM 700 confocal microscope (Zeiss). All samples intended for direct comparison were imaged using the same confocal settings.

Image Processing and Measurements

All images were processed and analyzed using standard ImageJ (Fiji) measurement tools. For 2D quantification of VL3 and VL4 muscles, z-projections of confocal images were used. VL3 and VL4 cell areas were traced by hand, based on phalloidin labeling. Outlines were used to record shapes (aspect ratio; cell width/cell length), sizes (areas), and positions (coordinates) of individual cells. To determine NMJ length, we generated binary images of anti-Discs large labeling and recorded area and position of the NMJ in relation to VL3 and VL4 cells. Automated thresholding of fluorescence intensities of anti-Lamin and/or Hoechst labeling was used to generate binary images of VL nuclei. We recorded the number, size (areas), and position (centroids) of all nuclei within each cell, and we used the binary images as masks to measure Hoechst and H3K9ac fluorescence intensities (sum intensity of pixel density). Further, nuclear centroids were used to calculate nearest neighbor distances and perform Voronoi tessellation (Du et al., 2010). Automated thresholding of anti-Fibrillar labeling was used to generate binary images of nucleoli and measure nucleolar sizes (areas). For calculation of DNA content, we normalized Hoechst fluorescence intensities of each muscle nucleus to diploid Adult Muscle Progenitors (AMPs) (Figeac et al., 2010) from the same larva. Work from the Orr-Weaver, Spradling and others labs routinely use DNA stains to estimate DNA content and ploidy (e.g. Dej and Spradling, 1999; Losick et al., 2013, 2016; Sher et al., 2013; Unhavaithaya and Orr-Weaver, 2012). Note that the extent of genome replication in polyploid cells has been published for several *Drosophila* tissues; it is known that not all genomic sequences are equally replicated, as an example, the heterochromatin (20-30% of the genome) is not replicated in tissues like the larval salivary gland and midgut (Nordman et al., 2011). Likewise, it has been determined that in larval salivary gland cells, ovarian follicle cells, and pupal trichogen cells, but not nurse cells, that rRNA genes are not fully replicated. As an example, salivary gland cells contain only one-fourth to one-eighth the expected number of rRNA genes (reviewed in Spradling and Orr-Weaver, 1987).

For 3D measurements of VL cell and nuclei, we determined the average depth/thickness of each cell and of all nuclei from one representative experiment. Volumes were calculated by multiplying thickness values with area measurements.

Simulation of Random Nuclear Positioning

To simulate random positioning of nuclei within VL muscle fibers, we used actual cell parameters of 200 wild-type cells (width, height, number of nuclei) and positioned nuclei randomly following uniform distributions. To assess the influence of stochasticity on our results, we repeated this procedure 1000 times. We calculated mean nearest neighbor distances and standard deviations for VL3 and VL4 nuclei +/- SD. The fits of Gaussians to the data (thick lines) were computed using the measured mean and SD.

Simulation of Nuclear Positioning

We simulated the positioning of N equally sized nuclei in a rectangular domain that interact with each other and with the cell sides via an isotropic pushing force, decreasing with distance. To underscore the differences between VL3 and VL4 cells, only cells from hemisegments 1-4 were used. Since we are working in a low Reynolds number regime, we can assume a friction-dominated environment, i.e. the velocities of the nuclei are proportional to the forces acting on them. Since we are only interested in equilibrium positions, we can rescale in order to normalize the coefficient of the internuclear interactions to 1. We assume the position of the centroid of the i -th nucleus follows

$$\frac{d}{dt}X_i(t) = \sum_{j=1, j \neq i}^N f(d_{ij})N_{ij} + \sum_{k=L,R,U,D}^N qf(d_{ik})N_{ik},$$

where d_{ij} is the distance between centroids i and j , N_{ij} is the vector of length 1 pointing from nucleus j to nucleus i . For the interactions with the sides, we define d_{ik} as the shortest distance between the i -th nucleus and the side with index k (L=left, R=right, U=upper, D=down) and N_{ik} is the unit vector normal to that side pointing towards the i -th nucleus. The scalar function $f(d)>0$ is a distance dependent pushing force and q is a free parameter describing the ratio between internuclear and nucleus-side forces. We used $f(d)=1/d$ and $f(d)=1/d^2$. To directly compare with the data, we used the same cell widths, heights, and number of nuclei as measured for the experimental data. As initial conditions the real positions were used, since this allows the use of the mean distance between the real and final (equilibrium) positions of the nuclei as an error functional in the simulation. This error was minimized with respect to q . Here only the results using $f(d)=1/d^2$ are shown, which gave a better fit with the data. The error functional was minimal for $q=0.7$. To simulate, we used Matlab's ode solver *ode15*, a variable-step, variable-order solver.

Simulation of Space-Sensing

We simulated the distribution of a signaling molecule, that is produced at a constant rate everywhere in the cell and diffuses until it is absorbed by a nucleus. For each cell, the real geometry and nuclear positions were used with nuclear radii of 3.8µm. Mathematically,

we solve the Poisson equation in 2D within each cell using Neumann boundary conditions at the cell membrane and Dirichlet boundary conditions at the nuclear envelope, i.e. if $s(x)$ is the concentration of the signal at position x , we solve

$$\begin{aligned}\Delta s &= -1, x \in C \\ s &= 0, x \in \partial N \\ \nabla s \cdot n &= 0, x \in \partial C,\end{aligned}$$

where ∂N denotes the union of all the boundaries of all nuclei and ∂C is the cell boundary. We solve using a Finite Element Method with an adaptive mesh utilizing Matlab's PDE toolbox. The amount of signal each nucleus receives, S , was calculated as the integral of the fluxes at its boundary. We assumed a linear relationship between the amount of signal received and the area of the nucleus A :

$$A = A_{min} + \alpha S.$$

We fitted the parameters A_{min} (the minimal nuclear area) and α (the sensitivity) to maximize the correlation between simulated and measured nuclear sizes, yielding $A_{min}=83 \mu\text{m}^2$ and $\alpha=0.044 \mu\text{m}^2$ per unit signal. For more information see [Methods S1](#).

Larval Locomotion Assay

Third instar larvae were placed in the center of a 10 cm apple juice plate (stained with green food color for better contrast) and recorded for 1 minute using an iPhone SE (Apple) on a custom mount. Each genotype was analyzed in 2 independent experiments; per individual experiment, a minimum of 10 larvae was analyzed. Movies of larval locomotion were processed and quantified in ImageJ using the trackmate plugin. Average velocities (+/- standard deviation) per genotype.

QUANTIFICATION AND STATISTICAL ANALYSIS

Sample sizes were chosen based on previous experience in the laboratory. Each experiment was performed in 2 technical replicas; per individual experiment a minimum of 4 larvae (biological replicates) and at least 8 VL muscles per larva were analyzed. For wild-type analyses, we quantified a total of 102 VL3 and 97 VL4 muscles from three control genotypes (w^{1118} , *Dmef2-GAL4;UAS-2xEGFP*, *Dmef2-GAL4;UAS-GFP RNAi*). Two-tailed Student's *t*-test and correlation coefficients (*R*) were computed using GraphPad Prism version 7.0a for Mac (GraphPad Software).

Unsupervised Multidimensional Cluster Analysis

Analysis was performed in R statistical language ([Team, 2013](#)). Data was clustered using classical multidimensional scaling (MDS) using *cmdscale* function with Euclidean distances and default parameters.

Multiple Linear Regression Analysis

To allow for direct comparison of the data and assess which parameters best predict nuclear sizes, we normalized all parameters (see below). The best prediction gave the following linear regression model: normalized (norm.) nuclear area = $a + b$ (norm. Voronoi area) + c (norm. distance to center). Where norm. nuclear area = nuclear area divided by the mean nuclear area in each cell; norm. Voronoi area = Voronoi area divided by the mean Voronoi area in each cell; norm. distance to center is defined between 0 (center) and 1 (poles). We fitted coefficients a, b, c of the linear regression model, yielding $a=0.87$, $b=0.31$, $c=-0.33$. *p*-values are well below 1% for both variables. $R^2=0.477$. Note that norm. Voronoi area and norm. distance to center are not correlated with each other ($R=-0.082$).

Developmental Cell, Volume 49

Supplemental Information

**Nuclear Scaling Is Coordinated
among Individual Nuclei
in Multinucleated Muscle Fibers**

Stefanie E. Windner, Angelika Manhart, Amelia Brown, Alex Mogilner, and Mary K. Baylies

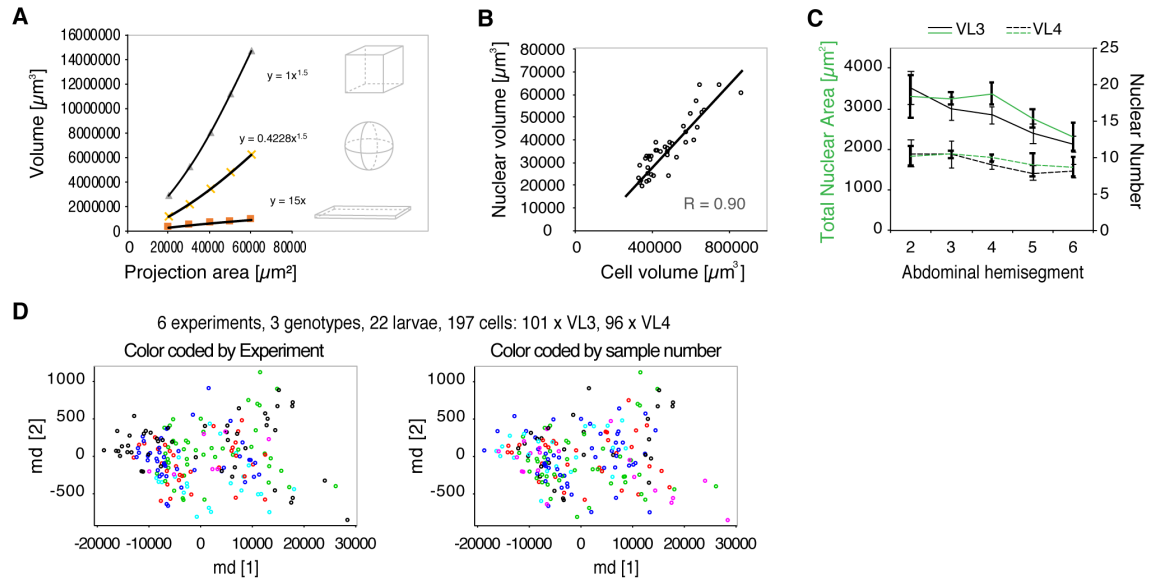


Figure S1. Quantification of VL cell and nuclear sizes. Related to Figure 1

(A) Relationships between volume and area measurements change with the shape of a 3D object. For flat VL muscles, increases in cell area correlate with only minor changes in cell volume compared to other cell shapes.

(B) Scatter plot of cumulative nuclear volume and VL cell volume, showing a similar global scaling relationship than quantification in 2D. n (cells) = 42, n (nuclei) = 572.

(C) Number of VL3 (solid lines) and VL4 (dashed lines) nuclei (black) and cumulative nuclear area (green) plotted against the corresponding abdominal hemisegment positions along the larvae. Lines represent mean values; error bars show standard deviation. $n_{\text{VL3}} = 102$, $n_{\text{VL4}} = 97$.

(D) Unsupervised multidimensional cluster analysis of VL muscles from 3 different genetic control backgrounds (w^{1118} , *Dmef2-GAL4*; *UAS-2xEGFP*, *Dmef2-GAL4*; *UAS-GFP RNAi*, two experimental replicates each) using the following parameters: cell size, cell shape (aspect ratio), nuclear number, total nuclear area, axis level (abdominal hemisegment number). Cells cluster in 2 groups, which clearly correspond to the VL3 and VL4 muscles (Figure 1J but show no bias for experimental replicate (left) or individual larvae (right)). $n_{\text{VL3}} = 102$, $n_{\text{VL4}} = 97$.

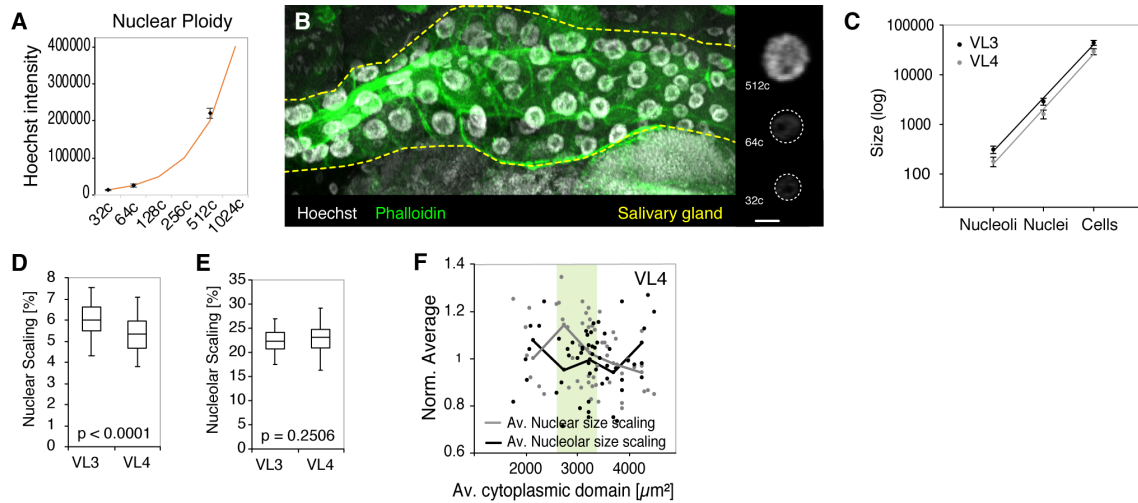


Figure S2. Muscle nuclei establish precise global scaling with cell size. Related to Figure 2.

(A, B) Comparison of DNA content in VL nuclei and other polyploid nuclei in the *Drosophila* larvae. Similar to previous publications (Frawley and Orr-Weaver, 2015), our method of calculating nuclear DNA content resulted in salivary gland nuclei ($n=10$) containing a minimum of 512c. Salivary gland and corresponding nuclei were labeled with phalloidin (green), and Hoechst (gray), respectively.

(C) Cumulative nucleolar and nuclear sizes scale linearly with cell size on a log scale.

(D, E) Boxplots comparing global nuclear scaling (D) (% nuclear area per cell) and global nucleolar scaling (E) (% nucleolar area per cell) in VL3 and VL4 muscles ($n_{VL3}=54$, $n_{VL4}=54$). Medians, 27/75 percentiles, min/max values. Both scaling parameters are significantly lower in VL4 muscles (p values indicate Student's t test result).

(F) Nuclear size scaling and nucleolar size scaling plotted against the average size of the cytoplasmic domains within VL4 cells (for VL3, see Figure 2O). Note: highest nuclear scaling values are associated with optimal cytoplasmic domain sizes (green area), while smaller or larger domain sizes correlate with increased nucleolar scaling and proportionally smaller nuclei. ($n_{VL3}=54$, $n_{VL4}=54$)

Scale bar, 25 μ m (B).

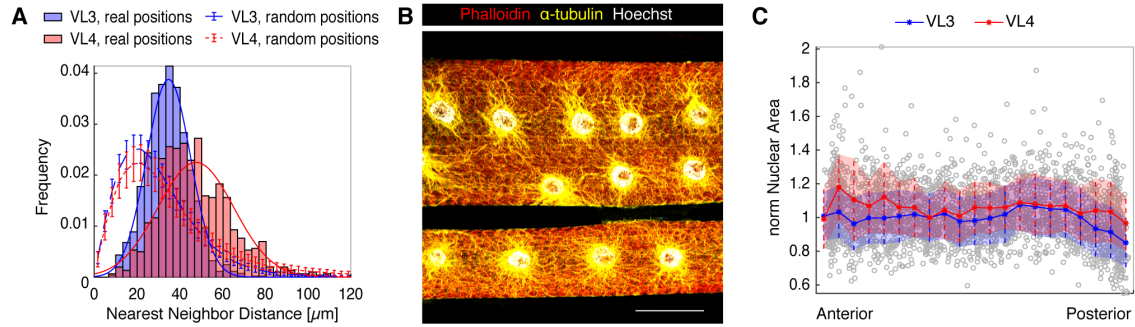


Figure S3. Nuclear positioning regulates individual nuclear sizes. Related to Figure 3.

(A) Histogram of Nearest Neighbor Distances (NNDs) in VL3 (blue) and VL4 muscles (red) in comparison to random distribution of nuclei (for simulation details see methods). NNDs follow normal distributions (blue and red lines) with mean \pm SD: 34.8 \pm 10.3 and 47.6 \pm 17.7 for VL3 and VL4 muscles, respectively.

(B) VL3 and VL4 muscles labeled with phalloidin (red) and anti- α -tubulin antibodies. Nuclear DNA (Hoechst) is shown in white. Scale bar: 50 μm .

(C) Distribution of normalized Simulated Nuclear Areas (Simulated Nuclear Area*No. of Nuclei/Cell Area) along the cell length (see Figure 3D and Mathematical Supplement for simulation details). Thick lines show averages, shaded regions correspond to standard deviation.

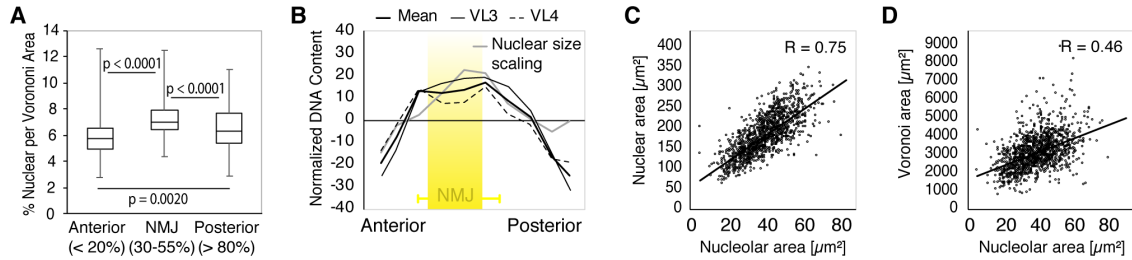


Figure S4. Local scaling of nuclear size, DNA content, and nucleolar size. Related to Figure 4.

(A) Box plot comparing median nuclear size scaling (% nuclear area per Voronoi domain) at the anterior and posterior MTJs (20% of cell length) and the NMJ (30-55% of cell length). p values determined by Student's t test.

(B) Normalized nuclear DNA content plotted against cell length. Mean values for VL3 and VL4 muscles are indicated. Gray line shows normalized nuclear size scaling for reference. NMJ region (yellow box) as in (Figure 4B).

(C,D) Scatter plots demonstrating local scaling of nucleolar areas with nuclear areas (D) ($R=0.75$) and with Voronoi domain areas (E) ($R=0.46$).

Sample numbers: $n=950$ nuclei (A), $n=1286$ nuclei (B-D)

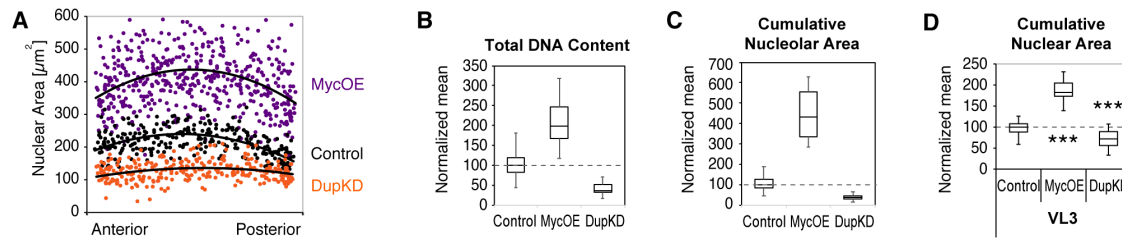


Figure S5. Muscle specific manipulations of nuclear DNA content. Related to Figures 5 and 6.

(A) Scatter plots showing distribution of nuclear areas along the long cell axis.

(B-D) Boxplots (whisker, min/max values; boxes, 25/75 percentiles) showing median cumulative DNA content, nucleolar area, and nuclear area in VL3 muscles of Cdt1(Dup)KD, Myc OE, and control larvae. Student's t test results are $p < 0.0001$ for both genotypes in (H-J)

Sample numbers: Control, $n_{\text{VL3}}=28$, $n_{\text{VL4}}=35$ cells; Cdt1(Dup)KD, $n_{\text{VL3}}=39$, $n_{\text{VL4}}=35$ cells; MycOE, $n_{\text{VL3}}=18$, $n_{\text{VL4}}=19$ cells

Supplemental Data File S1: Supplement to Figure 3

Simulation of space-sensing

Nuclear Scaling is coordinated among individual nuclei in multinucleated muscle fibers.

S. Windner, A. Manhart, A. Brown, A. Mogilner, M. Baylies

1 Space-sensing Model Details

Here, we provide details on the space-sensing model presented in the main text. In short, we suggest a mechanism which allows nuclei to sense the size of the space around them and adjust their size accordingly. The shape of larval muscle cells VL3 and VL4 is roughly a cuboid with typical dimensions

$$\text{width} \times \text{length} \times \text{depth} = 70\mu m \times 500\mu m \times 13\mu m,$$

i.e. the cells are very flat. Nuclei have the shape of flat cylinders, or discs, all positioned on one of the broad cuboids faces. We started by describing the 2D model, in which we neglect the cells' depths; the 3D variant of the model is described below. We hypothesized that a signal molecule, with concentration $s(x, y, t)$ at position (x, y) and time $t > 0$, is produced randomly anywhere in the cell with a constant rate γ . We also hypothesized that the signal molecules diffuse with diffusion constant D . If a molecule encounters a nucleus, it is taken up or absorbed by the nucleus. At each time instant, the nucleus adjusts its size, A according the total amount of signal it receives. The nuclear size, A , denotes the 2D area of the disc shaped nucleus, however since the nuclei are very flat and their depth was not observed to be variable, the nuclear area is proportional to its volume (see main Fig. 1).

To explore this model mathematically, we formulated the following system of differential equations:

$$\begin{aligned} \partial_t s &= D\Delta s + \gamma & (x, y) \in \mathcal{C}, \\ \nabla s \cdot n &= 0 & (x, y) \in \partial\mathcal{C}, \end{aligned} \tag{1}$$

$$s = 0 \quad (x, y) \in \bigcup_{i=1}^N \partial\mathcal{N}_i. \tag{2}$$

Here \mathcal{C} denotes the 2D cell excluding the space occupied by the nuclei and $\partial\mathcal{C}$ is the outer boundary. The vector n is the outward unit normal along this boundary. The nuclei

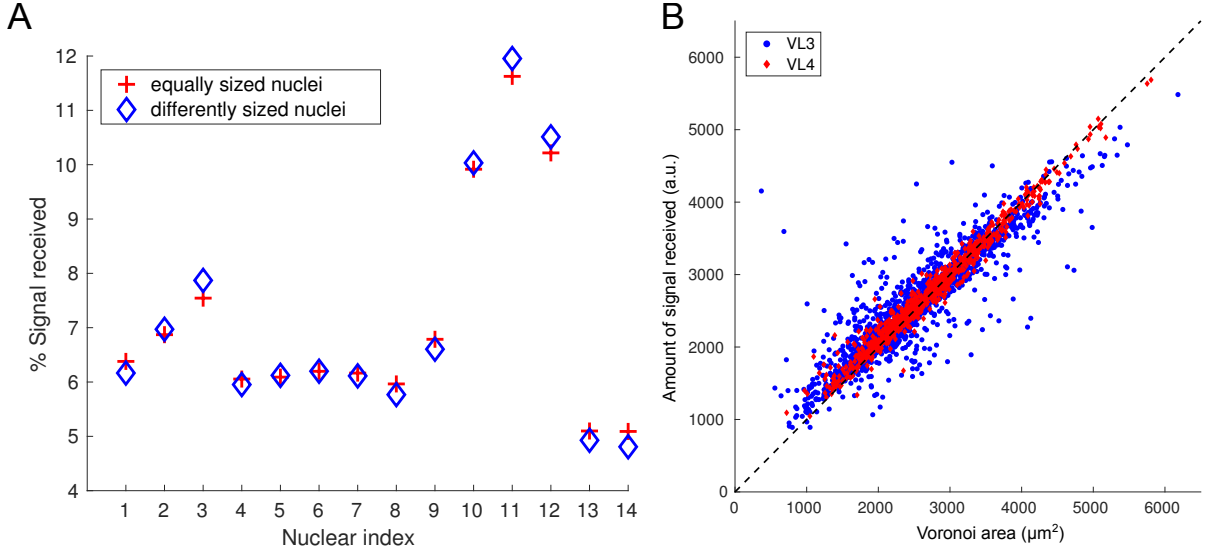


Figure M1: *A*: For the example cell shown in Fig. M2, we compared the % of the total amount of absorbed signal received by each nucleus if we solve (5) for equally sized nuclei ($45\mu\text{m}^2$), or having different sizes (using the measured nuclear areas). As can be seen, the difference is less than 0.5%. *B*: Comparing the geometrically determined Voronoi areas with the amount of signal received, calculated by using (5) and (3).

are indexed with $i = 1, \dots, N$ and $\partial\mathcal{N}_i$ is the boundary of the i -th nucleus. The first and second terms in the right hand side of the first equation describe the signal molecule diffusion and activation (or synthesis) with rate γ , respectively. The second equation is the no flux boundary condition at the cell boundaries, and the third equation is the absorption boundary condition at the circular nuclear boundaries.

The amount of signal the i -th nucleus receives per unit time is given by the curve integral:

$$S_i = -D \int_{\partial\mathcal{N}_i} \nabla s \cdot n \, d\Gamma_i, \quad (3)$$

where n is the unit normal pointing from the cell towards the nucleus. For the area of the i -th nucleus, A_i , we assume that:

$$\dot{A}_i = aS_i + b(A_{\min} - A_i). \quad (4)$$

The first term on the right-hand-side describes the growth of the nuclear area proportional to the amount of the signal, S_i , received per unit time. The second term is based on the assumption that, in the absence of any signal, the size of the nucleus approaches the minimal size, A_{\min} .

The steady state approximation. If we assume that the signal dynamics take place on a time scale faster than that of the nuclear growth, which is reasonable, then we can

at each time step approximate (1) by its steady state solution:

$$0 = D\Delta s + \gamma \quad (x, y) \in \mathcal{C}, \quad (5)$$

and iterate between solving this steady state equation and updating the nuclear sizes according to (4). After such simulations, we observed that the amount of signal each nucleus received, S_i , depended only very mildly on its size – and thereby time – but rather depended almost exclusively on its fixed position (see Fig. M1A). This observation justifies the following procedure to determine the nuclear equilibrium sizes: 1. Set a fixed initial nuclear area for all nuclei and solve (5) with this geometry to obtain the signal concentration $s(x, y)$. 2. Calculate the amount of signal each nucleus receives S_i per unit time using (3). 3. Calculate the equilibrium nuclear areas as the steady state solutions to (4), i.e.

$$A_i = A_{\min} + \frac{a}{b} S_i.$$

To obtain the minimal nuclear area A_{\min} and the signal sensitivity $\alpha = a/b$, we solved the associated least-squares problem of the overdetermined system, i.e. we determined A_{\min} and α so that the error between the measured and predicted nuclear areas in the Euclidean norm becomes minimal. This yielded $A_{\min} = 83\mu m^2$ and $\alpha = 0.044\mu m^2$ per unit signal. The average relative error between the predicted and actual nuclear area was 16.9%.

Note that setting $D = \gamma = 1$ does not affect the result, and so we used these parameters and methods to obtain the results shown in all modeling figures in the main text. For the simulations, we used the Finite Element Method with quadratic elements and the adaptive mesh solver provided by Matlab’s PDE Toolbox. We used the actual measured cellular outlines, positions and number of nuclei for 200 wild-type cells.

Results and interpretation. In our space-sensing model, the total amount of the signal produced (and hence also absorbed) per unit time is proportional to the total cell area. Since we assumed a linear dependence of the nuclear area on the amount of the signal received, the total predicted nuclear area increases linearly with cell area, as reported in the main text, Fig. 2G. However, our model goes beyond this cell-wide regulation of the nuclear area, since it suggests a mechanism for a local regulation of nuclear areas within each cell. This local regulation was evident in the experimental data if we normalized both nuclear areas and Voronoi areas by their per-cell-averages. We found that the local differences in the nuclear areas correlated with local differences in the Voronoi areas ($R = 0.45$, $p < 0.0001$). The amount of signal received by each nucleus, according to our model, was highly correlated with the size of its Voronoi domain (Fig. M1B, $R = 0.93$, $p < 0.0001$). Our model thereby offers a mechanistic explanation for both the cell-wide and some of the within-cell variation of the observed nuclear sizes. However, our space-sensing model does not explain why we see such a large dependence of nuclear size on nuclear distance to the cell poles (main text Fig. 3G). Reasons could lie in differences in signal production and/or signal transport near the poles.

Space-sensing for modified endoreplication. In the main text we discussed the effect of manipulating a muscle cell’s ability to increase its DNA copy number through endoreplication. In particular we looked at mutants where endoreplication was reduced through a knock-down (KD) of Ctd(Dup), and mutants where endoreplication was increased through overexpression (OE) of Myc. In the following we refer to them as KD and OE cells. We used our space-sensing model to determine the minimal nuclear area A_{\min} and the signal sensitivity α for KD and OE cells and found the following changes compared to the wild-type:

- For OE cells both A_{\min} and the sensitivity α roughly doubled (A_{\min} increased by 106%, α increased by 87%).
- For KD cells A_{\min} decreased by 11%, whereas α stayed roughly the same (< 1% increase).

The differences in A_{\min} might reflect the changes in (minimal) space requirements for more/less DNA copy numbers, whereas the increased sensitivity for OE cells could mean that OE nuclei react more sensitively to received signals compared to wild-type cells.

2 Variants of the Space-Sensing Model

Several variants of the space-sensing model presented above are possible. As already discussed, solving the fully time-dependent problem has a negligible effect on the final result.

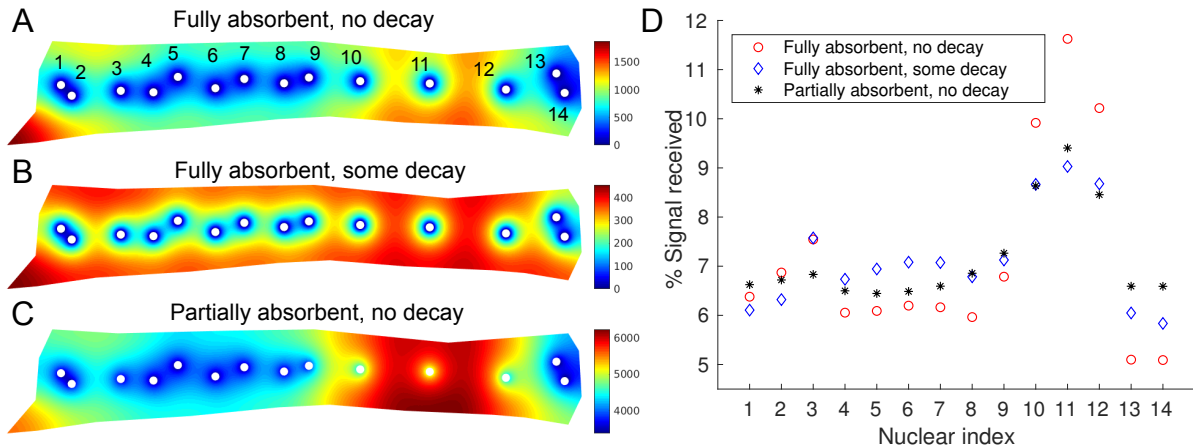


Figure M2: A-C: *Equilibrium signal distribution for three variants of the space-sensing model as described in the text. All three models use $D = \gamma = 1$. For A we used the basic model (fully absorbent, no decay). For B, we used $\delta = 0.002$, for C we used $\sigma = 0.03$. Note that the colorbars differ between A-C. D: Shown is the % of the total amount of absorbed signal received by each nucleus for the example cell and the models shown in A-C.*

Signal decay. As noted above, the amount of signal received according to the above model corresponded very well to the Voronoi areas of the nuclei. In the main text, Fig. 3F shows that the correlation between the nuclear areas and the Voronoi areas becomes sublinear for large Voronoi areas, i.e. the nuclei that are far away from their neighbors are slightly smaller than the great size of their Voronoi areas would suggest. We tested mathematically if this could be due to a slow spontaneous decay of the molecular signal. Since, for large Voronoi areas, the signal takes longer to reach the nucleus, a greater part of the signal would decay before reaching the nucleus, compared to smaller Voronoi areas, which could explain the observed sublinearity. Mathematically, this means replacing (1) by

$$\partial_t s = D\Delta s + \gamma - \delta s \quad (x, y) \in \mathcal{C},$$

where we assume a decay rate δ with units of per time. We tested different values of parameter δ and found that the average relative error stayed above 16%, i.e. we could not get a significantly better prediction of the nuclear size. However, when looking at the nuclei having the largest 2% of Voronoi areas in our sample, the average relative error between simulated and measured nuclear area dropped from 30.5% to 25.0% for a moderate amount of signal decay ($\delta = 0.0005$), as expected.

If the value of δ is chosen to be too large, the prediction becomes worse, since all nuclei receive roughly the same amount of signal, independent of the space around them. Fig. M2A,C shows that away from the nuclei, the signal distribution is more even, when there is the assumed decay. Fig. M2D compares how the percentage of obtained signal varies for the two cases. As expected, signal decay leads to less variation in the signal per nucleus within a cell.

Finite nuclear signal uptake speed. In the model described above, we assumed that all of the signal molecules that reach a nucleus are immediately taken up or absorbed. However, it is also reasonable to assume that there is a finite absorption rate σ . This would change the boundary condition (2) to

$$D\nabla s \cdot n = \sigma s \quad (x, y) \in \bigcup_{i=1}^N \partial\mathcal{N}_i.$$

The original model can be seen as limiting case for $\sigma \rightarrow \infty$. We performed tests with different values of σ and found that as long as σ is large enough, the general result was hardly affected. We were not able to obtain significantly better fits between the calculated and the measured nuclear area by varying σ . Fig. M2A,C shows the different signal distribution for an example cell using finite and infinite nuclear signal uptake speed and Fig. M2D compares how the percentage of obtained signal varies for the two cases. As can be observed, finite signal changes the overall signal distribution and also leads to less variation in the signal per nucleus within a cell.

Space-sensing in 3D. Next, we explored how solving in three space-dimensions affects the solution. Since nuclei are positioned on one surface of the muscle cell, we can model

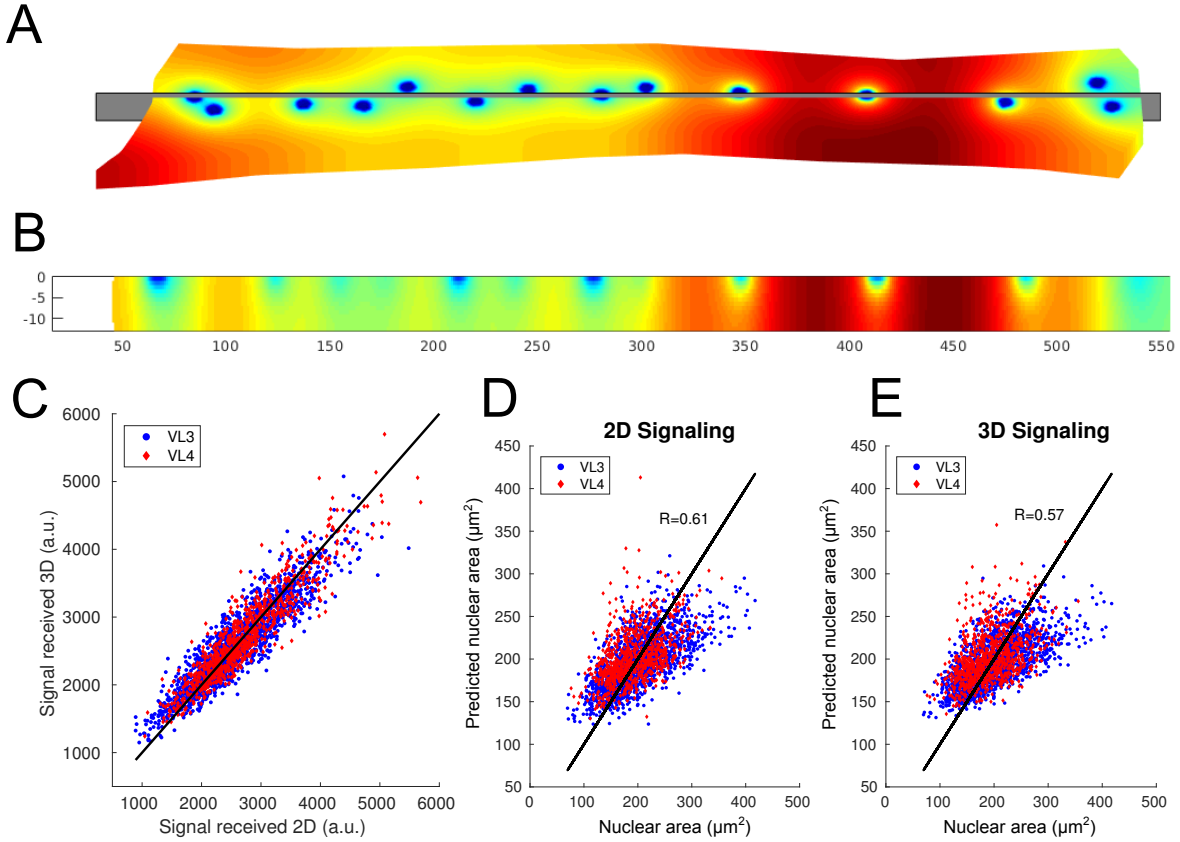


Figure M3: *A*: Signal distribution on the surface of a 3D cell as described in the text. Blue = low concentration, red = high concentration. *B*: Slice through the cell along the plane shown in *A*. *C*: Comparing the amount of signal received for 2477 nuclei between the 2D and the 3D model. *D-E*: Predicted vs measured nuclear areas of the 2D and 3D model.

them in the 3D setting by changing the boundary condition on that face from impenetrable (Neumann boundary condition) to fully absorbent (Dirichlet boundary condition) wherever there is a nucleus. Mathematically this means solving the following system of equations:

$$\begin{aligned}
 0 &= D\Delta s + \gamma & (x, y, z) \in \mathcal{C}, \\
 \nabla s \cdot n &= 0 & (x, y, z) \in \partial\mathcal{C} \cap \bigcup_{i=1}^N \mathcal{N}_i, \\
 s &= 0 & (x, y, z) \in \bigcup_{i=1}^N \mathcal{N}_i,
 \end{aligned} \tag{6}$$

where now \mathcal{N}_i are *filled* 2D discs, representing the nuclei. Figures M3A and B show the signal distribution on the surface of the cell and along a cut through the cell, respectively. As expected, signal amounts are low near the nuclear discs. Upon comparing the amounts of signal per nucleus between the 2D and 3D simulation in Fig. M3C, we see that they are very similar. Using the amount of signal received according to the 3D simulation still allows predicting the measured nuclear area very well, however, slightly less well than

using the 2D simulation. A speculative explanation could be that due to the sarcomeric structures in the cell, the diffusing signal cannot actually access the full depth of the cell.

3 Future Space-sensing Models

Active signal transport. So far the signal movement described was purely passive. However, it is possible that the signal is being transported actively, e.g. along microtubule tracks towards the nuclei or through the cell. This could be included in our model in a straight-forward manner.

Space-sensing in mammalian muscle cells. The geometry of mammalian skeletal muscles differs significantly from those of the fruit fly cells that we studied. Mammalian skeletal muscle cells form long, thin cylinders which contain myofibrils, within which the force-generating sarcomers are located. Muscle nuclei are positioned near the outer surface of the cylinder. Previous work [1] suggests that the position of the nuclei is consistent with a repulsion model similar to that presented in the main text. Our space-sensing model could be easily adapted to mammalian muscles, when data on correlations between nuclear sizes and spacing in such muscles become available. The different geometry could lead to different scaling laws: For example the signaling molecule could be diffusing in the full 3D cylinder or merely close to its 2D surface. Additionally, signal uptake could cause a linear increase in either nuclear volume or surface area, and finally also signal leakage from the nuclei could affect potential scaling laws.

References

- [1] Bruusgaard J, Liestøl K, Ekmark M, Kollstad K, Gundersen K. Number and spatial distribution of nuclei in the muscle fibres of normal mice studied in vivo. *J of Physiol.* 2003;551(2):467–478.